Ship-based MAX-DOAS measurements of tropospheric NO₂, SO₂, and HCHO distribution along the Yangtze River

Qianqian Hong[1,#], Cheng Liu[1,2,3,4,#,*], Ka Lok Chan[5,*], Qihou Hu[1], Zhouqing Xie[1,2,3,4], Haoran Liu[2], Fuqi Si[1], Jianguo Liu[1,3]

[1]Key Lab of Environmental Optics and Technology, Anhui Institute of Optics and Fine Mechanics, Hefei Institutes of Physical Science, Chinese Academy of Sciences, Hefei, 230031, China

[2]School of Earth and Space Sciences, University of Science and Technology of China, Hefei, 230026, China

[3]CAS Center for Excellence in Regional Atmospheric Environment, Institute of Urban Environment, Chinese Academy of Sciences, Xiamen, 361021, China

[4]Anhui Province Key Laboratory of Polar Environment and Global Change, USTC, Hefei, 230026, China

[5]Remote Sensing Technology Institute (IMF), German Aerospace Center (DLR), Oberpfaffenhofen, Germany

[#]This two authors contributed equally

[*]*Correspondence to*: Ka Lok Chan (ka.chan@dlr.de), Cheng Liu (chliu81@ustc.edu.cn)

Abstract. In this paper, we present ship-based Multi-Axis Differential Optical Absorption Spectroscopy (MAX-DOAS) measurements of tropospheric trace gases distribution along Yangtze River during winter 2015. The measurements were performed along Yangtze River between Shanghai and Wuhan covering major industrial areas in eastern China. Tropospheric vertical column densities (VCDs) of nitrogen dioxide (NO_2), sulfur dioxide (SO_2), and formaldehyde (HCHO) were retrieved using air mass factor calculated by radiative transfer model. Enhanced tropospheric NO_2 and SO_2 VCDs were detected over downwind areas of industrial zones over Yangtze River. In addition, spatial distributions of atmospheric pollutants are strongly affected by meteorological conditions, i.e., positive correlations were found between concentration of pollutants and wind speed over these areas indicating strong influence of transportation of pollutants from high-emission upwind areas along Yangtze River. Comparison of tropospheric NO_2 VCDs between ship-based MAX-DOAS and OMI satellite observations shows good agreement with each other with Pearson correlation coefficient (R) of 0.82. In this study, NO_2/SO_2 ratio was used to estimate the relative contributions of industrial sources and vehicle emissions to ambient NO_2 levels. Analysis results of NO_2/SO_2 ratio shows that higher contribution of industrial NO_2 emissions in Jiangsu province, while NO_2 levels in Jiangxi and Hubei provinces are mainly related to vehicle emissions. These results indicate that different pollution control strategies should be applied in different provinces. In addition, multiple linear regression analysis of ambient carbon monoxide (CO) and odd oxygen (O_x) indicated that the primary emission and secondary formation of HCHO contribute $54.4 \pm 3.7\%$ and $39.3 \pm 4.3\%$ to the ambient HCHO, respectively. The largest contribution from primary emissions in winter suggested that photochemically induced secondary formation of HCHO is reduced due to lower solar

irradiance in winter. Our findings provide an improved understanding of major pollution sources along the eastern part of Yangtze River which are useful for designing specific air pollution control policies.

1 Introduction

Nitrogen dioxide (NO_2), sulfur dioxide (SO_2), and formaldehyde (HCHO) are important atmospheric constituents playing important roles in tropospheric chemistry. Nitrogen oxides (NO_x), defined as the sum of nitric oxide (NO) and NO_2, is one of the major pollutant in the troposphere, playing a key role in both tropospheric and stratospheric chemistry. It takes part in the catalytic formation of tropospheric ozone (O_3), while being a catalyst for the destruction of stratospheric O_3 (Crutzen, 1970). Major sources of NO_x are high-temperature combustions (e.g. fossil fuel burning, biomass burning) and natural processes (e.g. soil microbial activity, lightning events (Lee et al., 1997)). NO_2 in high concentration is harmful to human health, especially for immune and respiratory systems. In addition, NO_2 can lead to the formation of nitrate aerosols, which is an important component of fine suspended particles in the urban environment. Sulfur dioxide (SO_2) is the most abundant anthropogenic sulfur containing air pollutant. In urban areas, SO_2 is produced mainly through the combustion of sulfur-containing fossil fuels for power generation and domestic heating, which accounts for more than 75% of the total SO_2 emissions (Chin et al., 2000). Atmospheric SO_2 causes similar environmental problems as NO_2, such as acidification of the natural aqua system, formation of secondary aerosols and causing negative impacts on human health (Chiang et al., 2016). The atmospheric lifetime of both NO_2 and SO_2 are relatively short, ranging from few hours up to few days (Krotkov et al., 2016), therefore, their spatial distributions are highly influenced by the emission sources.

Formaldehyde (HCHO) is one of most abundant volatile organic compounds (VOCs) in the atmosphere, playing an important role in air quality and atmospheric photochemistry. Incomplete combustion processes including industrial emissions and vehicle exhaust have been identified as the major HCHO sources in the urban atmosphere (Garcia et al., 2006). Formaldehyde can also be produced from the atmospheric photochemical oxidation of methane (CH_4) and non-methane hydrocarbons (NMHCs) (Miller et al., 2008). In the polluted regions, terminal alkenes such as isoprene, ethene and propene are the most important HCHO precursors (Goldan et al., 2000). The major sinks of HCHO are photolysis, reaction with OH radical and wet deposition in the atmosphere (Lei et al., 2009). The short atmospheric lifetime of HCHO under sunlight is typically very short (2-4 h), indicating that the daytime ambient HCHO are mostly produced locally (Arlander et al., 1995).

Multi-Axis Differential Optical Absorption Spectroscopy (MAX-DOAS) is a passive remote sensing technique providing indispensable information of atmospheric aerosols and trace gases (Platt and Stutz, 2008). Information of tropospheric trace gases are obtained from the molecular absorption in the ultraviolet and visible wavelength bands by applying the differential optical absorption spectroscopy (DOAS) method to the observations of scattered sun light spectra in several different viewing directions. This method has been widely used for atmospheric NO_2, SO_2, and HCHO in the past decades (Lee et al., 1997;Heckel et al., 2005;Wang et al., 2014;Hendrick et al., 2014;Chan et al., 2015). MAX-DOAS observations are not only limited to ground based application, but also can be performed on different mobile platforms like

cars (Johansson et al., 2009;Ibrahim et al., 2010;Shaiganfar et al., 2011), aircrafts (Baidar et al., 2013;Dix et al., 2016) or ships (Sinreich et al., 2010;Peters et al., 2012;Takashima et al., 2012;Schreier et al., 2015). In this study, ship-based MAX-DOAS measurements of NO_2, SO_2, and HCHO were performed along the Yangtze River. Previous ship-based MAX-DOAS measurements were mainly focused on remote and coastal marine environments to obtain boundary layer background concentrations of trace gases, such as in the Indian and Pacific Ocean. In this study, we performed ship-based MAX-DOAS observations along the Yangtze River, the busiest navigable inland waterway in the world to obtain insight spatial distribution information of trace gases in eastern China.

Yangtze River delta (YRD) is one of the most populated regions in China. Due to the rapid industrialization and urbanization in the past two decades, Yangtze River delta (YRD) is facing a series of air pollution problems. As emission sources are not well characterized and the atmospheric processes are rather complex, it is important to measure the spatial distribution of atmospheric pollutants, i.e., NO_2, SO_2, and HCHO, in YRD for the investigation of emission sources and atmospheric processes and provides scientific supports for the prevention and designing control measures of air pollution. In this study, spatial distribution of tropospheric NO_2, SO_2, and HCHO were retrieved from ship-based MAX-DOAS observations along the Yangtze River between Shanghai and Wuhan. The experiment aims to provide improved understanding of emission sources and atmospheric processes over eastern China, which is potentially useful for the formulation of strategic air pollution control and identification of the effectiveness of air pollution control policies.

In this paper, we present ship-based Multi-Axis Differential Optical Absorption Spectroscopy (MAX-DOAS) measurements of tropospheric trace gases distribution along the Yangtze River during winter 2015. The measurements were performed along the Yangtze River between Shanghai and Wuhan covering the major industrial areas in eastern China. Details of the experimental setup, spectral analysis and trace gases retrieval of the ship-based MAX-DOAS measurement is presented in section 2. Comparison with OMI NO_2 and the contribution of major emission sources to NO_2 levels along the Yangtze River, as well as the contribution of primary and secondary sources of HCHO are shown in section 3.

2 Methodology

2.1 The Yangtze River measurement campaign

The Yangtze River campaign took place in winter 2015 along the Yangtze River over eastern China within the framework of the "Regional Transport and Transformation of Air Pollution in Eastern China". The aims of Yangtze River campaign are to provide better understanding of the transportation and transformation of atmospheric pollution, and to identify the potential impacts on air quality and climate.

Ship-based measurement campaign was carried out along the eastern part of Yangtze River between Shanghai and Wuhan. The campaign includes a departing journey (from Shanghai to Wuhan) and a returning journey (from Wuhan to Shanghai). The measurement campaign started on 21 November 2015 at 19:30 LT from Shanghai (31.36°N, 121.62°E), a major industrial and commercial hub of eastern China, and arrived in Wuhan (30.62°N, 114.32°E) on 29 November 2015 at

95 15:42 LT. The measurement ship was then directly sailing back and finally arrived in Shanghai on 4 December 2015 at 20:30 LT. The journey covered most of the major industrial areas in eastern China including several population dense metropolitan cities, such as Nanjing, Wuhu, and Jiujiang. Detail of the cruise track is shown in Fig. 1.

The ship-based MAX-DOAS instrument was part of the air quality monitoring framework of the Yangtze River measurement campaign. The instrument was installed at the beginning of the measurement campaign and started to provide
100 atmospheric observations on 22 November 2015. A summary of the meteorological conditions during the Yangtze River campaign are shown in Table 1.

2.2 MAX-DOAS measurements

2.2.1 Experimental setup

Ship-based MAX-DOAS measurements were performed during Yangtze River campaign. The ship-based MAX-DOAS
105 instrument was developed at the Anhui Institute of Optics and Fine Mechanics (AIOFM), Chinese Academy of Sciences (CAS) which consists of a telescope, a spectrometer and a computer acting as controlling and data acquisition unit. Viewing directions of the telescope are controlled by a stepping motor, scattered sunlight collected by the telescope is redirected to the spectrometer for spectral analysis through an optical fiber bundle. The field of view of the telescope is estimated to be less than 1°. An imaging spectrometer (Princeton instrument), equipped with a charge-coupled device (CCD) detector (512 ×
110 2048 pixels) is used to measure spectra in the ultraviolet (UV) wavelength range from 303 nm to 370 nm with a spectral resolution of 0.35 nm full width half maximum (FWHM). Spectral data recorded by the imaging spectrometer were average along the first dimension of the CCD in order to get a better signal to noise ratio. During the measurement campaign, the viewing azimuth angle of the telescope was adjusted to 90° (right) relative to the heading direction of the ship (see Fig. S1). A full measurement sequence includes elevation angles (α) of 30° and 90° (zenith). The exposure time of each measurement
115 is set to 100 ms.

2.2.2 Data processing and filtering

Although the instrument was positioned in front of the exhaust stack (see Fig. S1), the MAX-DOAS measurements could still be influenced by the exhaust from the ship. Therefore, measurement data contaminated by the ship exhaust were filtered out in our analysis. Individual measurements taken under unfavorable wind directions (relative wind directions
120 between 150° and 270° with respect to the heading of the ship) were discarded in the following analysis. Due to the stronger absorptions of stratospheric species and low signal to noise ratio at large SZAs, only measurements with solar zenith angle smaller than 75° were taken into account for the DSCDs retrieval. With these filtering criterions (unfavorable wind directions and SZAs), 5.4% and 15.8% of all data were rejected before DSCDs retrieval, respectively.

As the viewing elevation angles of the measurements were relatively high (30° and 90°), therefore, they are insensitivity

125 to the instability or the movement of the ship. In addition, the exposure time of a measurement is rather short (100 ms), the change of measurement elevation and azimuth angle during one measurement is negligible.

2.2.3 DOAS retrieval

Differential slant column densities (DSCDs) of trace gases are derived from the measurement spectra by applying the differential optical absorption spectroscopy (DOAS) technique (Platt and Stutz, 2008). In this study, MAX-DOAS spectra

130 are analyzed using the QDOAS spectral fitting software suite developed by BIRA-IASB (http://uv-vis.aeronomie.be/software/QDOAS/). The wavelength calibration was performed by using a high resolution solar reference spectrum (Chance and Kurucz, 2010). Dark current (DC) spectrum was taken with exposure time of 3000 ms and number of scan of 20 scans while electronic offset spectrum (OFFSET) was taken with exposure time of 3 ms and number of scan of 20000 scans. The dark current and offset spectra were used to correct measurement spectra prior to the spectra analysis.

135 Several trace gas absorption cross sections (Vandaele et al., 1998;Vandaele et al., 2009;Meller and Moortgat, 2000;Serdyuchenko et al., 2014;Thalman and Volkamer, 2013;Fleischmann et al., 2004), the Ring spectrum, a Frauenhofer reference spectrum and a low order polynomial are included in the DOAS fit. Details of the DOAS fit settings are shown in Table 2. In this study, zenith measurement spectrum with the lowest pollutant concentration was selected as the Frauenhofer reference spectrum for the retrieval of measurement spectra taken during the measurement campaign. Similar reference

140 spectrum selection approaches have been used in different mobile measurements studies (Wu et al., 2013;Li et al., 2015).

Figure 2 shows an example of the DOAS analysis of a spectrum recorded on 1 December 2015 at 14:02 LT with an elevation of 30°. The retrieved NO_2 (Fig. 2a), SO_2 (Fig. 2b), and HCHO (Fig. 2c) DSCDs are 1.40×10^{17}, 6.25×10^{16}, and 3.51×10^{16} molec/cm^2, respectively. In this study, only data with root mean square (RMS) of residuals smaller than 3.0×10^{-3} are considered. This filtering criterion (RMS) removed 18.7%, 20.2%, and 25.2% of data for NO_2, SO_2, and HCHO,

145 respectively.

2.2.4 Determination of the tropospheric VCD

The DOAS spectral retrieval results are the differential slant column densities (DSCDs) which are defined as the difference between the slant column density (SCD) of the measured spectrum and the Frauenhofer reference spectrum:

$$DSCD_{meas} = SCD_{meas} - SCD_{Fraunhofer} \tag{1}$$

150 The SCD is the integrated trace gas concentration along the light path through the atmosphere, which includes both tropospheric and stratospheric part ($SCD_{meas} = SCD_{trop} + SCD_{strat}$). As scattering of photons most likely takes place in the troposphere, it can be assumed that the light path in the stratosphere for zenith and off zenith measurements are very similar, i.e. $SCD_{strat}(\alpha) \approx SCD_{strat}(90°)$. Then Eq. (1) can be written as:

$$DSCD_{meas}(\alpha) = (SCD_{trop}(\alpha) + SCD_{strat}(\alpha)) - (SCD_{trop}(90°) + SCD_{strat}(90°))$$
$$= SCD_{trop}(\alpha) - SCD_{trop}(90°) \qquad (2)$$
$$= DSCD_{trop}(\alpha)$$

155 where $DSCD_{trop}(\alpha)$ represents the tropospheric DSCD measured at elevation angle of α.

As the measured DSCDs are dependent on the absorption path in the atmosphere, the measurement has to convert to vertical column density (VCD) in order to compare with each other. For this purpose, a concept so-called air mass factor (AMF) is applied (Solomon et al., 1987), and the tropospheric vertical column density (VCD_{trop}) can be expressed as follows:

$$VCD_{trop} = \frac{SCD_{trop}(\alpha)}{AMF_{trop}(\alpha)} \qquad (3)$$

160 Assuming scattering happens above the trace gas layer, the AMF for the zenith and the off-axis view can be estimated as 1 and $1/\sin\alpha$, respectively (Hönninger et al., 2004). This method is so-called "geometric approximation". However, geometric approximation of AMF could result in large errors under high aerosol load conditions (Wagner et al., 2007). In addition, relative azimuth angle, defined as the angle between the viewing direction and the sun, also plays an important role in the AMF calculation. This effect is particularly important for mobile observations (Wagner et al., 2010). For this reason, we
165 adapted the simultaneous lidar measurement of aerosol profiles for the radiative transfer calculation of AMFs.

In this study, AMFs for SCD to VCD conversion were calculated using the radiative transfer model SCIATRAN 2.2 (Rozanov et al., 2005). Compared to the geometric approach, radiative transfer calculation of AMF is more computational expensive. Vertical distribution profiles of aerosols and trace gases are also important for the AMF calculation. In this study, trace gas profiles (e.g., O_3, NO_2, SO_2, and HCHO) and vertical profiles of pressure and temperature are taken from the
170 Weather Research and Forecasting model coupled with Chemistry (WRF-Chem) simulations for AMF calculations (Liu et al., 2016). Atmospheric profiles obtained from the model simulation were then interpolated in both spatial and temporal dimension to MAX-DOAS measurements location and time for AMF calculation. Hourly averaged aerosol extinction coefficients in the lowest 2 km of the troposphere were taken from the Mie lidar measurements while aerosols above 2 km were not considered in the radiative transfer simulations. Aerosols below the lidar overlap height are considered to be
175 homogeneous in the AMF calculation. In order to estimate the influence of aerosol above 2 km on the AMF calculation, we compared AMFs calculated with and without considering aerosols above 2 km. As the lidar measurement above 2 km has larger uncertainty, aerosols extinction information above 2 km is taken from WRF-Chem simulations. Comparison results show that AMFs calculated with considering aerosol above 2 km are on average 2-4% lower than AMFs without considering aerosol at upper altitudes. The result indicates that ignoring aerosols above 2 km only cause a negligible error on the AMF
180 calculation. Tropospheric AMFs of NO_2, SO_2, and HCHO were calculated at the central wavelength of their DOAS fitting windows which are 354 nm, 311 nm, and 347 nm, respectively. The aerosol extinction profiles obtained from the Mie lidar are converted to MAX-DOAS retrieval wavelengths assuming a fix Ångström coefficient (Ångström, 1929) of 1. The aerosol extinction profiles at 354 nm, 311 nm, and 347 nm can be derived using the following formula:

$$\alpha(\lambda_x, z) = \alpha(\lambda_{532}, z) \times (\frac{\lambda_x}{\lambda_{532}})^{-\upsilon} \tag{4}$$

185 where $\alpha(\lambda_x, z)$ is the aerosol extinction coefficient at wavelength λ_x; $\alpha(\lambda_{532}, z)$ is the aerosol extinction coefficient at 532 nm; υ is the Ångström coefficient which is assigned to a fix value ($\upsilon=1$) in this study.

A fix set of single scattering albedo (SSA) of 0.95, asymmetry parameter of 0.68 and surface albedo of 0.06 is assumed in the radiative transfer calculations (Chen et al., 2009;Pinker et al., 1995). In this study, all radiative transfer calculations were performed by using the radiative transfer model SCIATRAN 2.2 (Rozanov et al., 2005). Previous studies show that the

190 uncertainties caused by aerosol single scattering albedo (SSA), aerosol asymmetry parameter (AP) and surface albedo assumptions are less than 10% (Chen et al., 2009;Wang et al., 2012b). Uncertainty of lidar measurement of aerosol extinction profiles also contributes to the uncertainty in the AMF calculations. A sensitivity study was performed with aerosol profiles with different AODs (i.e., 0.4, 0.6, 0.8, 1.0, and 1.2) and a single trace gas profile with a constant NO_2, SO_2, and HCHO concentration of 5.4×10^{11} molecules cm^{-3} (equal to 20 ppb at the ground level) to quantify the uncertainty

195 caused by aerosol profiles used in the AMF calculation at different wavelengths. In the sensitivity analysis, aerosols and trace gases are assumed well mixed in the lowest 0.8 km, following an exponential decrease with height. The result shows that the variation of AMFs with different aerosol profiles (SZAs smaller than 75°) are 11%, 13%, and 11% for NO_2, SO_2, and HCHO, respectively (see Fig. S2). Considering the uncertainties caused by the assumptions of SSA, AP and surface albedo and uncertainties of aerosol load in the radiative transfer calculations, we estimated the uncertainties of tropospheric

200 AMFs are ranging between 30-43% for SZAs smaller than 75°.

As the DOAS analysis results are DSCDs, we have to apply the concept of differential air mass factor (DAMF) to convert the measurement to vertical columns as follows:

$$\begin{aligned} DSCD_{trop}(\alpha) &= SCD_{trop}(\alpha) - SCD_{trop}(90°) \\ &= VCD_{trop} \times AMF_{trop}(\alpha) - VCD_{trop} \times AMF_{trop}(90°) \\ &\Rightarrow VCD_{trop} = \frac{DSCD_{trop}(\alpha)}{AMF_{trop}(\alpha) - AMF_{trop}(90°)} = \frac{DSCD_{trop}(\alpha)}{DAMF_{trop}(\alpha)} \end{aligned} \tag{5}$$

where DAMF is defined as the difference of air mass factor (AMF) between $\alpha \neq 90°$ and $\alpha = 90°$

205 ($DAMF_{trop}(\alpha) = AMF_{trop}(\alpha) - AMF_{trop}(90°)$). This equation (Eq. 5) is regard as the standard method for the determination of the tropospheric trace gas VCDs from MAX-DOAS observations.

Mobile MAX-DOAS observations are strongly influenced by rapid change of air masses and radiative transfer conditions along the navigating route. The standard method (Eqs. 1 to 5) to calculate tropospheric VCDs can result in large errors. An alternative method has been suggested for mobile MAX-DOAS measurements (Wagner et al., 2010). This method

210 has been applied in previous mobile MAX-DOAS observations (Ibrahim et al., 2010;Wu et al., 2015) and reported to be better than the standard method for mobile platforms. Therefore, we adapted the new method in this study for tropospheric VCDs conversion. The VCD_{trop} can be expressed as follows (combining Eqs. 1 and 3):

$$VCD_{trop} = \frac{SCD_{meas}(\alpha) - SCD_{strat}(SZA)}{AMF_{trop}(\alpha)}$$

$$= \frac{DSCD_{meas}(\alpha) + SCD_{ref} - SCD_{strat}(SZA)}{AMF_{trop}(\alpha)} \tag{6}$$

where SZA denotes the solar zenith angle. We refer to the difference of the two unknowns SCD_{ref} and SCD_{strat} (SZA) as $DSCD_{offset}$(SZA) and can be written as follows:

$$DSCD_{offset}(SZA) = SCD_{ref} - SCD_{strat}(SZA) \tag{7}$$

The expressions for VCD_{trop} in Eqs. 5 and 6 are set equal:

$$\frac{DSCD_{meas}(\alpha) - DSCD_{meas}(90°)}{AMF_{trop}(\alpha) - AMF_{trop}(90°)}$$

$$= \frac{DSCD_{meas}(\alpha) + SCD_{ref} - SCD_{strat}(SZA)}{AMF_{trop}(\alpha)} \tag{8}$$

This equation can be solved for $DSCD_{offset}$(SZA) as defined in Eq. 7:

$$DSCD_{offset}(SZA)$$

$$= \frac{AMF_{trop}(90°) \times DSCD_{meas}(\alpha) - AMF_{trop}(\alpha) \times DSCD_{meas}(90°)}{AMF_{trop}(\alpha) - AMF_{trop}(90°)} \tag{9}$$

Since $DSCD_{offset}$(SZA) is a smooth function of the SZA or time, we can fit the time series of calculated $DSCD_{offset}$(SZA or t_i) by a low order polynomial (second order). t_i indicates the time between the two selected measurements from one elevation sequence i, the time series of the calculated $DSCD_{offset}$(SZA) can be written as:

$$DSCD_{offset}(t_i)$$

$$= \frac{AMF_{trop}(90°, t_i) \times DSCD_{meas}(\alpha, t_i) - AMF_{trop}(\alpha, t_i) \times DSCD_{meas}(90°, t_i)}{AMF_{trop}(\alpha, t_i) - AMF_{trop}(90°, t_i)} \tag{10}$$

The fitted polynomial represents the approximation of $DSCD_{offset}(t_i)$ and can be inserted into Eq. 8. In this way we can obtain a time series of tropospheric trace gas VCDs essentially without errors introduced by the spatio-temporal variations of the trace gas field (example is shown in Figs. S3-5). The detailed description of the method can be found in Wagner et al. (2010).

2.3 OMI Satellite observations

The Ozone Monitoring Instrument (OMI) was launched onboard the NASA Earth Observing System (EOS)-Aura satellite on 15 July 2004 (Levelt et al., 2006). It is a nadir-viewing imaging spectrometer measuring direct and Earth's reflected sunlight in the ultra violet (UV) and visible (VIS) range from 270 to 500 nm. OMI aims to monitor global atmospheric trace gases distribution with high spatial (up to 13 × 24 km) and temporal (daily global coverage) resolution. The local overpass time of OMI is between 13:40 and 13:50 (local time) on the ascending node. In this study, USTC's OMI tropospheric NO_2 product is used, which is developed based on OMI's primary product and has proven to be more suitable

235 for the atmospheric conditions in China (Liu et al., 2016;Xing et al., 2017;Su et al., 2017). Slant column densities (SCDs) of NO_2 are retrieved by applying the DOAS fit to OMI spectra (data source: OMI Level 1B VIS Global Radiances Data product (OML1BRVG) (https://disc.gsfc.nasa.gov/Aura/data-holdings/OMI/oml1brvg_v003.shtml)). Separation of stratospheric and tropospheric columns is achieved by the local analysis of the stratospheric field over unpolluted areas (Bucsela et al., 2013;Krotkov et al., 2017).The OMI NO_2 SCDs are converted to VCDs by using the concept of air mass factor (AMF). The

240 AMFs are calculated based on the NO_2 and atmospheric profiles derived from WRF-Chem chemistry transport model simulations with a horizontal resolution of 20×20 km over eastern China (17-49 °N, 95-124°E) and 26 vertical layers from the ground level to the height with a pressure of 50 hPa. In this study, the National Centers for Environmental Prediction (NCEP) Final operational global analysis (FNL) meteorological data are used to drive the WRF-Chem simulations. Details of the chemistry transport model simulation as well as the satellite data retrieval process can be found in Liu et al. (2016).

245 **2.4 Ancillary data**

Lidar observations of aerosol vertical distribution were also carried out during the campaign. The lidar system is equipped with a diode-pumped frequency doubled Nd:YAG laser emitting laser pulses at 532 nm. The typical pulse energy of the laser is about 20 mJ with a pulse repetition frequency of 20 Hz. The laser beam is emitted with divergence of 1 mrad and 200 mm off-axis to the receiving telescope with a field of view of 2 mrad, resulting in an overlap height of about 195 m.

250 A constant lidar ratio (S_p, extinction to backscatter ratio) of 50 sr was assumed in the lidar retrieval. Details of the lidar system and the data retrieval can be found in (Chen et al., 2017;Fan et al., 2018).

Meteorological parameters such as wind direction and wind speed were obtained from an automatic weather station on board the measurement ship. In-situ trace gas measurements, such as CO, O_3, and NO_2 were performed using Sensor Networks for Air Quality (SNAQ) during the campaign. SNAQ is a highly portable and low-cost air quality measurement

255 network methodology incorporating electrochemical gas sensors which can be used for high resolution air quality studies at ppbv levels (Mead et al., 2013). CO, O_3, and NO_2 were monitored by SNAQ with a 20s resolution, and the detection limit of CO, O_3, and NO_2 were 3 ppbv+5% of measured CO, 2 ppbv+5% of measured O_3, and 2 ppbv+5% of measured NO_2, respectively, and in special cases 5% of measured values can increase to 10%.

3 Results and discussion

260 MAX-DOAS measurements were conducted during the campaign period from 22 November to 4 December 2015. The measurements were interrupted occasionally due to power failure of the measurement ship and instrumental problems, details of the measurement period are listed in Table 1. All the times reported herein are local time (LT=UTC+8). Measurement spectra taken during daytime between 08:00 and 16:00 (SZAs smaller than 75°), corresponding to the sunshine period during wintertime in China were used for analysis. In order to avoid unnecessary uncertainties introduced during the

265   VCD conversion, we use the radiative transfer model with lidar aerosol profiles as input for the AMF calculation to convert all the measurements to VCDs.

3.1 General characteristics of tropospheric NO_2, SO_2, and HCHO

Time series of tropospheric NO_2, SO_2, and HCHO vertical column densities (VCDs) for the entire campaign from 22 November to 4 December, 2015 are shown in Figs. 3-4. Missing data are due to power failure of the measurement ship and 270 instrumental problems, measurements taken under unfavorable wind directions and SZAs larger than 75°. The mean NO_2 VCD of the entire campaign is 2.27×10^{16} molec/cm^2, with an exceptionally large variation range from 1.31×10^{15} molec/cm^2 to 7.72×10^{16} molec/cm^2. About half of the NO_2 VCDs are in the range of 5-20 ($\times 10^{15}$ molec/cm^2) and high NO_2 VCDs (i.e., $> 5 \times 10^{16}$ molec/cm^2, about the 95th percentile value) are about 2.2 times higher than mean value (Fig. S6a). The mean SO_2 VCD of the entire campaign is 2.14×10^{16} molec/cm^2 with a range from 1.05×10^{15} molec/cm^2 to 9.29×10^{16} molec/cm^2. 275 Although more than half of the values are in the range of 10-25 ($\times 10^{15}$ molec/cm^2), high SO_2 VCDs (i.e., $> 5.5 \times 10^{16}$ molec/cm^2, about the 95th percentile value) are about 2.5 times higher than mean value (Fig. S6b). It should be noted that three elevated tropospheric NO_2 and SO_2 VCDs events have been observed which are highlighted in gray in Fig. 4. Pollution events were identified with both NO_2 and SO_2 VCDs reached or above the threshold value of 4.0×10^{16} molec/cm^2. The mean HCHO VCDs of the entire campaign is 9.61×10^{15} molec/cm^2, ranging from 1.05×10^{15} molec/cm^2 to 5.37×10^{16} 280 molec/cm^2. Most of the HCHO VCDs lie between 1-14 ($\times 10^{15}$ molec/cm^2) and high HCHO VCDs (i.e., $>2.6 \times 10^{16}$ molec/cm^2, about the 95th percentile value) are about 2.7 times higher than mean value (see Fig. S6c).

The spatial distribution of NO_2, SO_2, and HCHO VCDs along the eastern part of the Yangtze River are shown in Fig. 5. Three elevated tropospheric NO_2 and SO_2 VCDs events over Yangtze River were detected around three major industrial cities with large number of heavy emission sources, i.e., Jiujiang (#1), an industrial city located on the southern shores of the 285 Yangtze River in northwest Jiangxi Province, China; Nanjing (#2), the provincial capital and the most populous city in Jiangsu province, Eastern China; and Shanghai (#3), a metropolis located in the Yangtze River Delta with the busiest container port in the world.

The variations of the NO_2 and SO_2 VCDs are closely linked to the spatial distribution of emission sources around industrial cities as well as meteorological conditions (e.g., wind speed and wind direction). Most of the previous studies 290 show an inverse relationship between wind speed and air quality, i.e., the lower the wind speed the higher the pollution level, which suggesting that low wind speed condition is limiting the mixing and dispersion of atmospheric pollutants, and thus in favors of accumulation of local emissions (Chan et al., 2012;Wang et al., 2012b;Chan et al., 2014;Chan et al., 2017;Wang et al., 2017). However, positive correlations ($p < 0.05$, t-test) were found between the mobile MAX-DOAS NO_2 and SO_2 VCDs (red circle and blue square, respectively) and wind speed during these three events (Fig. 6a-6c). The result suggested that 295 these episodes are most likely not related to accumulation of local emission. We further investigated the possible influence of transport on the NO_2 spatial distribution by looking into the backward trajectories during these episodes. We calculated

24h backward trajectories of air masses using the HYSPLIT (Hybrid Single-Particle Lagrangian Integrated Trajectory) model which is developed by the National Oceanic and Atmospheric Administration-Air Resource Laboratory (NOAA-ARL) (Stein et al., 2015) (http://ready.arl.noaa.gov/HYSPLIT.php). Meteorological data from the Global Data Assimilation System (GDAS) with a spatial resolution of $1° \times 1°$ and 24 vertical levels was used in the model for the trajectory simulations. The 24h backward trajectories (green markers indicate the trajectory point of −6, −12, −18 and −24 h) were calculated for each hour during three pollution episodes using the NOAA HYSPLIT model with end point altitude of 500 m a.g.l.. The result is shown in Fig. 6d. As indicated by the 24h back-trajectories, NO_2 VCDs on 1 December 2015 (Event #1) are prominent when under southwesterly wind condition. This is probably due to an industrial city (Jiujiang) is located on the southern shores of the Yangtze River at the upwind areas of the ship. Backward trajectories (Events #2 and #3, Fig. 6d) indicated prevailing northwesterly wind during 3-4 December 2015. In addition, the backward trajectory analysis suggested that rapid transport of air masses carries significant amount of pollutants from polluted areas in northern China (Krotkov et al., 2016) across the Yangtze River, resulting in higher NO_2 and SO_2 VCDs. The higher the wind speed the higher the NO_2 and SO_2 VCDs under northwesterly wind conditions (Figs. 6b and 6c), which means that the transport from distant sources is more significant than of the contribution from local emission sources. These results suggested that the spatial distributions of pollutants along the Yangtze River are strongly influenced by the meteorological condition. In comparison to these high VCDs events, relatively low NO_2 and SO_2 VCDs were observed in the first few days of the campaign (22 to 25 November), which might due to occasional showers during these days removed pollutants through wet deposition.

Elevated tropospheric HCHO VCDs (up to 2×10^{16} molec/cm^2) are observed mostly during clear days (e.g., 26 November, 3 and 4 December), with good visibility and low cloud coverage (see Table 1). This is probably due to the enhancement of photochemical formation of atmospheric HCHO under strong solar irradiation. In contrast, lower HCHO VCDs were observed mainly on rainy, cloudy and haze days, which might be due to stronger wet deposition and weaker solar irradiation during these days. Elevated HCHO VCDs in the HCHO time series was found on 3 December 2015 when the ship was anchored at Yizheng Marine department (32.25°N, 119.15°E). This day is mostly cloud-free with good visibility. In addition, HCHO VCDs show a diurnal pattern with low values in the morning and late afternoon and peaks around noontime. This diurnal pattern indicates the significant contribution of photochemical formation of HCHO. Detailed analysis of the primary sources and secondary formation of HCHO for 3 December 2015 is shown in section 3.4.

3.2 Comparison with OMI NO_2

In order to compare the ship-based MAX-DOAS measurements to OMI observations, the ship-based MAX-DOAS data are temporally averaged around the OMI satellite overpass time from 12:00 to 14:00 (LT). For 22, 25, and 26 November, no MAX-DOAS data were available during the OMI overpass time due to power failure of the measurement ship and instrumental problems (see Table 1). All OMI measurement within 20 km (ship speed: ~10-20 km/h) radius of the ship's averaged position from 12:00 to 14:00 (LT) are averaged and compared to the averaged ship MAX-DOAS data. For 29

November and 1, 3 December, no satellite observations were available at the corresponding ship's location. As a result, 7
330   days (Nov 23, 24, 27, 28 and 30 and Dec 2 and 4) of measurements from both OMI and ship-based MAX-DOAS are used
for data comparison.

Scatter plot of the ship MAX-DOAS and OMI NO_2 measurements is shown in Fig. 7a. The NASA's OMI NO_2 VCDs
are also shown as reference. Compared to the NASA's standard product, the USTC's OMI tropospheric NO_2 VCD agrees
better with ground measurements a Pearson correlation coefficient (R) of 0.82 while the correlation between MAX-DOAS
335   and the NASA OMI product is 0.76. However, the regression analysis indicated that the USTC's and NASA's OMI data
underestimated the tropospheric NO_2 VCD by about 10% and 27%, respectively. Time series of ship-based MAX-DOAS
and OMI NO_2 VCDs is shown in Fig. 7b. The ship-based MAX-DOAS data were higher than the OMI values for most of the
time. Underestimation of tropospheric NO_2 VCDs for OMI might attribute to the averaging effect over large OMI pixel.
Unpolluted or less polluted areas are also included in the OMI pixel and resulting in low values over pollution hotspots.

340   In order to have a better insight of the spatial distribution pattern of tropospheric NO_2 along the Yangtze River, NO_2
VCDs measured by both ship-based MAX-DOAS and OMI are plot on same map which is shown in Fig. 8. OMI
tropospheric NO_2 VCDs are gridded onto a $0.02° \times 0.02°$ grid using the parabolic spline gridding algorithm (Kuhlmann et al.,
2014;Chan et al., 2015;Chan et al., 2017). The gridding routine was reported to provide more realistic continuous spatial
distributions of NO_2 while preserving the details of emission hotspots (Chan et al., 2015;Chan et al., 2017). During clear
345   days (27 November and 4 December, 2015), both ship-based MAX-DOAS and OMI capture similar NO_2 spatial pattern (Fig.
8a and 8d). However, a significant enhancement of NO_2 close to the exit of the Yangtze River was observed by ship-based
MAX-DOAS observation, as shown in Fig. 8d which does not show up in the OMI observation. This is probably due to the
mismatch of OMI overpass time and the ship-based MAX-DOAS measurement time. The spatial coverage of OMI
observation was limited on 30 November 2015 due to cloudy sky condition. On the other hand, NO_2 hotspots can be
350   observed from the ship-based measurement as shown in Fig. 8b. These NO_2 peaks cannot be detected by OMI as cloud
shield NO_2 at the lower troposphere. Different spatial patterns were detected by the ship-based MAX-DOAS and OMI
satellite on 2 December 2015 which was a haze day (Fig. 8c). In order to estimate the influence of ignoring aerosols in
satellite AMF calculation on NO_2 retrieval, we compared OMI NO_2 VCDs calculated with and without considering aerosol
in the satellite AMF calculations. Significant enhancement of OMI NO_2 VCDs is observed over some areas when aerosol is
355   considered in the satellite retrieval. However, the spatial pattern observed by ship MAX-DOAS and OMI are still quite
different. The result indicates the impact of aerosol could not fully explain the discrepancy between MAX-DOAS and OMI
on this day. On the other hand, the MAX-DOAS and OMI observations agree better during OMI overpass time (black star in
Fig. 8) and the agreement decay when the time differences between MAX-DOAS and OMI measurements become larger.
This implies a strong temporal variability of NO_2 on this day and leads to larger differences of NO_2 spatial distribution
360   between OMI and ship MAX-DOAS measurements.

Ship-based MAX-DOAS is more sensitivity to near surface NO_2, however, the measurement is only limited to the area
along the Yangtze River. In order to have a broader coverage of tropospheric NO_2 distribution over Yangtze River delta,

OMI tropospheric NO_2 product is used in this study. Figure 9 shows the averaged tropospheric NO_2 VCDs along Yangtze River and its surrounding regions (26°-34°N, 112°-124°E). Enhanced NO_2 VCDs appeared at the exit of Yangtze River. This area includes southern Jiangsu, eastern Anhui, and northern Zhejiang. It is obvious that the pollution level along Yangtze River (white line in Fig. 9) is higher than surrounding areas, especially areas from Wuhu to Wuhan. This is probably resulting from the fact that most of the industrial activities are concentrated along Yangtze River as the logistic is much more convenience and cost efficient through water transportation. Our observation implies that specific emission control measures should be applied on the highly polluted industry along Yangtze River.

3.3 Possible contributions to ambient NO_2 levels

Fossil fuel consumption is the major source of anthropogenic NO_x emissions, especially in highly industrialized and urbanized regions. Industrial sources (including power plants, other fuel combustion facilities, and non-combustion processes) and vehicle emissions are the two major contributors, which together composed about 90% of the total anthropogenic NO_x emissions in China (Huang et al., 2011;Shi et al., 2014). Understanding the individual contributions of industrial sources and vehicle exhaust to ambient NO_2 is important for designing suitable emission control strategies in polluted areas, like Yangtze River delta. In this study, we estimated contribution of different emission sources to NO_2 levels along the Yangtze River by analyzing the ratio between ambient NO_2 and SO_2.

Figure 1 (green dots) shows a number of power plants are located along the Yangtze River between Shanghai and Wuhan. Industrial zones can also be found close to these power plants along the Yangtze River due to the logistically convenience. Emissions of NO_2 and SO_2 from coal-fired power plants are significant air pollution sources. As the atmospheric lifetime of NO_2 and SO_2 is roughly the same (Krotkov et al., 2016), the ambient NO_2/SO_2 ratio is approximately equal to the emission ratio of NO_2/SO_2. In addition, vehicles mainly emit NO_x and their SO_2 emissions are trivial, while coal-fired power plants, heavy industries and ships mostly use sulfur-containing fossil fuels which emit both NO_x and SO_2. Therefore, lower NO_2/SO_2 ratio implies larger contribution from industrial sources (Zhang et al., 2017), while higher NO_2/SO_2 ratios indicate larger contribution from vehicle exhaust sources toward NO_2 levels (Mallik and Lal, 2014;Krotkov et al., 2016). It should be noted that it is difficult to separate local ship emissions from industrial emissions due to their similar emission components, so industrial sources in this paper including not only coal-fired power plants and heavy industries but also ship emissions. In this study, we analyzed NO_2/SO_2 ratios around coal-fired power plants along the Yangtze River. NO_2/SO_2 ratios are determined by linear regression of NO_2 and SO_2 measurements around power plants which is shown in Fig. 10. NO_2 and SO_2 VCDs measured within 2 km of the power plants (adjacent industrial zones and ships are included) are used for the analysis. Good correlation was found between NO_2 and SO_2 VCDs measured around coal-fired power plants (R = 0.91, N = 195) which implies the ambient NO_2 and SO_2 are mostly emitted from similar sources (i.e., coal combustion). The slope of linear regression is 0.56 ± 0.02. Relatively low NO_2/SO_2 ratio indicates large contributions from combustion of high sulfur containing fuel, e.g. coal, which is mainly used for power generation. In

395 addition, the desulfurization filters installed in these power plants are either ineffective or maybe even deactivated during the time.

Assuming the ambient NO_2 is mostly emitted from industrial sources (mainly from power plants, and ship emissions are also included) and vehicle exhaust, other anthropogenic sources like biomass burning and natural sources are negligible. The NO_2/SO_2 ratio (slope) and intercept (offset) of the linear regression of data measured around the power plants can be used to

400 estimate the source contributions of industrial sources and vehicle exhaust to the ambient NO_2 concentration. Assuming the NO_2/SO_2 ratio for industrial emission is constant, we can estimate the industrial and vehicle contribution by using the following equations:

$$P_{Industrial\ sources} = \frac{NO_2(power\ plants)}{NO_2(total)} \times 100\%$$
$$= \frac{SO_2 \times Slope + Intercept}{NO_2(total)} \times 100\%$$

(13)

$$P_{vehicle\ exhaust} = \frac{NO_2(vehicle\ exhaust)}{NO_2(total)} \times 100\%$$
$$= \frac{NO_2(total) - (SO_2 \times Slope + Intercept)}{NO_2(total)} \times 100\%$$

(14)

405 where SO_2 represents the SO_2 VCDs, NO_2(total) denotes the NO_2 VCDs, the slope and the intercept of the linear regression are 0.56 and 1.86 (unit: 10^{15} molec/cm^2), respectively.

During the campaign, the route covered four provinces along the Yangtze River, i.e., Jiangsu, Anhui, Jiangxi, and Hubei. Figure 11 shows the relative contributions of industrial sources and vehicle exhaust to the ambient NO_2 levels over the four provinces. In Jiangsu province, a higher contribution from power generation to NO_2 level was found, which is

410 mainly due to large number of power plant located along the Yangtze River in Jiangsu province. The NO_x emission over the eastern China, including Jiangsu province (15.41 t/(km^2·y)) (Shi et al., 2014), is more intensive than other parts of China. In addition, Jiangsu province is one of the province in China with maximum annual NO_x emissions from coal-fired power plants (Zhao et al., 2008;Wang et al., 2012a). In contrast, the contribution of vehicle exhaust to NO_2 level was higher than that of coal-fired power plants in Jiangxi and Hubei provinces, suggesting that traffic emissions have larger impacts on the

415 NO_2 level in these provinces. Previous study shows a dramatic growth of the number of vehicle plays an increasingly significant role for regional NO_2 pollution over past years (Xia et al., 2016). For Jiangxi and Hubei provinces, the number of power plant is less than Jiangsu province. Therefore, the contribution of vehicle exhaust to NO_2 level is expected to be more pronounced along with the dramatic growth of vehicle number. In Anhui province, the contributions of coal-fired power plants and vehicle exhaust to NO_2 level were about the same. Our result suggests that different pollution controlling strategy

420 should be applied in different province: power generation emissions are the major reduction target for Jiangsu province; while more specific control policies are need to reduce the vehicle exhaust pollution in Jiangxi and Hubei provinces.

3.4 Estimation of primary and secondary sources of ambient HCHO

Industrial zones are mainly located along the Yangtze River due to the logistically convenience. Observations along the Yangtze River were constantly influenced by plumes originating from various industrial activities, such as coal burning, crude oil refining and plastic and rubber syntheses. Besides the direct primary emissions, ambient HCHO can also formed through secondary atmospheric processes. Therefore, it is important to quantify the contribution of primary and secondary HCHO in order to better understand the atmospheric processes as well as the corresponding impacts on the local air quality.

CO is directly emitted to the atmosphere through combustion processes (e.g., incomplete combustion of vehicle engines) and therefore can be use as a tracer for primary emission of HCHO (Friedfeld et al., 2002;Garcia et al., 2006). On the other hand, O_3 reacts with NO emitted from automobiles to form NO_2. Thus, the odd oxygen O_x ($O_x = O_3 + NO_2$) is often used as a tracer for photochemical processes in urban atmosphere (Wood et al., 2010). In this study, we use CO as the tracer of primary HCHO while O_x being an indicator of secondary HCHO formation. The CO and O_x data were measured by Sensor Networks for Air Quality (SNAQ) during this campaign. In addition, a simplified formula was used to convert mean HCHO DSCDs to mixing ratios (ppbv) (Lee et al., 2008) (detailed formula and parameters are shown in the supplement). Previous study shows that a linear model can be used for the source appointment analysis of ambient HCHO (Garcia et al., 2006). The measured HCHO was apportioned by a multiple linear regression model which parameterized by the following equation:

$$[HCHO] = \beta_0 + \beta_1[CO] + \beta_2[O_x] \tag{15}$$

where β_0, β_1, and β_2 are the fit coefficients obtained from the multiple linear regression. The analysis was done in daily bases.

The relative contributions of primary emission, photochemical formation and atmospheric background HCHO to the total atmospheric HCHO are calculated according to the tracer concentrations and corresponding fit coefficients by the following equations:

$$P_{Primary} = \frac{\beta_1[CO]_i}{\beta_0 + \beta_1[CO]_i + \beta_2[O_x]_i} \times 100\% \tag{16}$$

$$P_{Secondary} = \frac{\beta_2[O_x]_i}{\beta_0 + \beta_1[CO]_i + \beta_2[O_x]_i} \times 100\% \tag{17}$$

$$P_{Background} = \frac{\beta_0}{\beta_0 + \beta_1[CO]_i + \beta_2[O_x]_i} \times 100\% \tag{18}$$

where $P_{Primary}$ represents the contribution from primary sources (vehicle and industrial emissions); $P_{Secondary}$ is the contribution of secondary HCHO (photochemical oxidation); and $P_{Background}$ indicates the background HCHO which is neither classified as primary nor secondary HCHO. According to previous studies in YRD (Wang et al., 2015;Ma et al., 2016), the background level of HCHO is limited to 1 ppbv. Therefore, the regression parameter β_0 is fixed at 1 ppbv in this analysis. $[CO]_i$ and $[O_x]_i$ represent the concentrations of CO and O_x at time i, respectively. β_1 and β_2 are the regression coefficients obtained from multiple linear regressions.

As other factors (e.g., meteorological conditions) can also affect the atmospheric HCHO concentration, in order to make

sure the regression model is representative for atmospheric conditions, only data fulfilling the following criteria are used in the analysis (a) correlation coefficient (R) larger than 0.75 (Li et al., 2010) and (b) significance value lower than 0.05. Of the 12 days of measurements, only 2 days fulfill the criteria to be considered in this analysis. The parameters of the multiple linear regression fit and the linear Pearson correlation coefficient (R) for the measured and modeled HCHO are shown in Table 3.

Time series of measured and modeled HCHO of 3 December 2015 is shown in Fig. 12a. Both the measured and modeled HCHO concentrations show similar temporal development with a rising trend in the morning and reached the peak value at noon, then followed by a decrease in the afternoon. The linear regression between measured and modeled HCHO shows a reasonably good agreement with slope of 0.98 and Pearson correlation coefficient (R) of 0.78 on December 3, 2015 (see Fig. 12b). All measurements lie within the 95% prediction interval indicating the best estimate of modeled HCHO. The regression model could not fully reconstruct the measurements, indicating there are other factors influencing the atmospheric HCHO levels. Due to the complexity of emission sources, a constant CO/HCHO factor might not be good enough to represent the HCHO emission from all primary sources. A number of petrochemical-related manufactures and organic synthesis processes industry located along the Yangtze River resulting in higher HCHO emissions and the CO emission factor varies with their emission processes. In addition, as we were measuring on a mobile platform, the composition of emission could change with the measurement location. Future investigation could focus on characterizing the primary industrial emissions of HCHO by different sector.

The diurnal variation of HCHO contribution from primary sources, secondary formation and background contributions on 3 December 2015 is shown in Fig. 13. Background HCHO only accounts for a small portion ($6.2 \pm 0.8\%$, average $\pm$ S.D.) of the total ambient HCHO, while the primary sources contribute the largest fraction of the ambient HCHO, with an average percentage of $54.4 \pm 3.7\%$. The primary sources contributions were relatively stable, which might be due to industrial emission does not show a significant diurnal pattern. The contribution associated with secondary formation accounted for roughly $39.3 \pm 4.3\%$ of the total HCHO on daily average. Secondary formation of HCHO shows two peak values around 10:00 LT and noon time (11:00-14:00 LT). The 24 h backward trajectories on 3 December (Fig. 6d) suggested that rapid transport of air masses carries significant amount of pollutants including formaldehyde precursor from polluted area in northern China. Thus, the peak of relative contribution of secondary sources around 10:00 LT is probably resulted from the transportation of formaldehyde precursor. On the other hand, the peak value of secondary formation of HCHO during noon time (11:00-14:00) is mainly due to enhancement of photochemical reaction during noon time. Our result is consistence with a similar study in Rome, Italy, which the secondary contribution of HCHO is about 35% during winter time (Possanzini et al., 2002). While secondary formation of HCHO has been reported as the largest ambient HCHO source in summer (Parrish et al., 2012;Ling et al., 2017). Reduced photochemical reaction in winter resulting in lower formation rate of HCHO, and therefore, primary emissions become the major source of ambient HCHO in winter.

4 Summary

485   In this paper, we present the ship-based MAX-DOAS measurements along Yangtze River from Shanghai to Wuhan (22 November to 4 December, 2015). Scattered sunlight spectra were measured to retrieve differential tropospheric slant column densities (DSCDs) of NO_2, SO_2, and HCHO. DSCDs of NO_2, SO_2, and HCHO were converted to tropospheric vertical column densities (VCDs) using AMF computed by Radiative Transfer Model with lidar aerosol profile as input. During the campaign, three significantly enhanced tropospheric NO_2 and SO_2 VCDs events were detected over the

490   downwind areas of industrial zones. Spatial distributions of atmospheric pollutants are strongly affected by meteorological conditions, i.e., positive correlations were found between the ship-based MAX-DOAS data and wind speed for these three events, which indicates that the transportation of pollutants from the high-emission areas have a strong influence on the NO_2 and SO_2 distribution along Yangtze River. Comparison of tropospheric NO_2 VCDs between ship-based MAX-DOAS and OMI satellite observations shows good agreement with Pearson correlation coefficient (R) of 0.82. However, OMI

495   underestimated tropospheric NO_2 by 10% which is mainly due to the averaging effect over large OMI pixels. In addition, satellite observations have lower sensitivity to near-surface pollutants compared to ground-based measurements.

     In this study, NO_2/SO_2 ratio is used to quantify relative contributions of industrial sources and vehicle emissions to ambient NO_2 levels. The result shows that Jiangsu province has a higher contribution from industrial sources due to the large number of power plants situated along the Yangtze River in Jiangsu. In contrast, contributions from vehicle emissions to

500   NO_2 level are higher than that of industrial sources in Jiangxi and Hubei provinces. Our result suggested that traffic volume has large impact on NO_2 level in these provinces. These results indicate that different NO_2 pollution control strategy should be applied in different provinces. In addition, we estimated the contributions of primary and secondary emission sources to ambient HCHO levels using a multiple linear regression method. Result from 3 December 2015 indicated that primary sources have the largest contribution to the ambient HCHO ($54.4 \pm 3.7\%$), while secondary formation contributes $39.3 \pm$

505   4.3% of the total ambient HCHO. The remaining fraction $6.2 \pm 0.8\%$ is attributed to the background. The largest contribution from primary sources in winter suggested that photochemically induced secondary formation of ambient HCHO is reduced due to lower solar irradiance in winter. This study provides an improved understanding of the impacts of different emission sources in different provinces along the eastern part of Yangtze River to the local air quality. Our findings are useful for designing specific air pollution control and environmental policies.

510   *Acknowledgement*

     The authors would like to thank Prof. Jianmin Chen's group from Fudan University for the organization of the Yangtze River measurement campaign. We would also like to thank the National Oceanic and Atmospheric Administration (NOAA) Air Resources Laboratory (ARL) for the provision of the HYSPLIT transport and dispersion model used in this publication. We thank Fudan University and Cambridge University in providing meteorological measurements and measurements of other

515   atmospheric trace pollutants. The work presented in this paper is jointly supported by the National Key Project of MOST

(project no. 2016YFC0203302, 2016YFC0200404), the National Natural Science Foundation of China (project no. 41575021, 91544212, 41722501, 51778596), Key Project of CAS (project no. KJZD-EW-TZ-G06-01) and the National Key R&D Program of China (project no. 2017YFC0210002).

References

520 Ångström, A.: On the atmospheric transmission of sun radiation and on dust in the air, Geografiska Annaler, 11, 156-166, 1929.

Arlander, D. W., Bruning, D., Schmidt, U., and Ehhalt, D. H.: The tropospheric distribution of formaldehyde during TROPOZ-II, Journal Of Atmospheric Chemistry, 22, 251-269, doi:10.1007/bf00696637, 1995.

Baidar, S., Oetjen, H., Coburn, S., Dix, B., Ortega, I., Sinreich, R., and Volkamer, R.: The CU Airborne MAX-DOAS

525   instrument: vertical profiling of aerosol extinction and trace gases, Atmospheric Measurement Techniques, 6, 719-739, doi:10.5194/amt-6-719-2013, 2013.

Bucsela, E., Krotkov, N., Celarier, E., Lamsal, L., Swartz, W., Bhartia, P., Boersma, K., Veefkind, J., Gleason, J., and Pickering, K.: A new stratospheric and tropospheric NO_2 retrieval algorithm for nadir-viewing satellite instruments: applications to OMI, Atmospheric Measurement Techniques, 6, 2607, 2013.

530 Chan, K., Ning, Z., Westerdahl, D., Wong, K., Sun, Y., Hartl, A., and Wenig, M.: Dispersive infrared spectroscopy measurements of atmospheric CO_2 using a Fabry-Pérot interferometer sensor, Science of the Total Environment, 472, 27-35, 2014.

Chan, K., Wiegner, M., Wenig, M., and Pöhler, D.: Observations of tropospheric aerosols and NO_2 in Hong Kong over 5 years using ground based MAX-DOAS, Science of The Total Environment,

535   doi:https://doi.org/10.1016/j.scitotenv.2017.10.153, 2017.

Chan, K. L., Pöhler, D., Kuhlmann, G., Hartl, A., Platt, U., and Wenig, M. O.: NO_2 measurements in Hong Kong using LED based long path differential optical absorption spectroscopy, Atmos. Meas. Tech., 5, 901-912, doi:10.5194/amt-5-901-2012, 2012.

Chan, K. L., Hartl, A., Lam, Y. F., Xie, P. H., Liu, W. Q., Cheung, H. M., Lampel, J., Poehler, D., Li, A., Xu, J., Zhou, H. J.,

540   Ning, Z., and Wenig, M. O.: Observations of tropospheric NO_2 using ground based MAX-DOAS and OMI measurements during the Shanghai World Expo 2010, Atmospheric Environment, 119, 45-58, doi:10.1016/j.atmosenv.2015.08.041, 2015.

Chance, K., and Kurucz, R.: An improved high-resolution solar reference spectrum for earth's atmosphere measurements in the ultraviolet, visible, and near infrared, Journal of quantitative spectroscopy and radiative transfer, 111, 1289-1295,

545   2010.

Chen, D., Zhou, B., Beirle, S., Chen, L. M., and Wagner, T.: Tropospheric NO_2 column densities deduced from zenith-sky DOAS measurements in Shanghai, China, and their application to satellite validation, Atmospheric Chemistry And

Physics, 9, 3641-3662, 2009.

Chen, Z., Liu, C., Liu, W., Zhang, T., and Xu, J.: A synchronous observation of enhanced aerosol and NO_2 over Beijing,
China, in winter 2015, Science Of the Total Environment, 575, 429-436, doi:10.1016/j.scitotenv.2016.09.189, 2017.

Chiang, T.-Y., Yuan, T.-H., Shie, R.-H., Chen, C.-F., and Chan, C.-C.: Increased incidence of allergic rhinitis, bronchitis and
asthma, in children living near a petrochemical complex with SO_2 pollution, Environment International, 96, 1-7,
doi:10.1016/j.envint.2016.08.009, 2016.

Chin, M., Rood, R. B., Lin, S. J., Muller, J. F., and Thompson, A. M.: Atmospheric sulfur cycle simulated in the global
model GOCART: Model description and global properties, Journal Of Geophysical Research-Atmospheres, 105, 24671-
24687, doi:10.1029/2000jd900384, 2000.

Crutzen, P. J.: The influence of nitrogen oxides on the atmospheric ozone content, Quarterly Journal of the Royal
Meteorological Society, 96, 320-325, 1970.

Dix, B., Koenig, T. K., and Volkamer, R.: Parameterization retrieval of trace gas volume mixing ratios from Airborne MAX-
DOAS, Atmospheric Measurement Techniques, 9, 5655-5675, doi:10.5194/amt-9-5655-2016, 2016.

Fan, S., Liu, C., Xie, Z., Dong, Y., Hu, Q., Fan, G., Chen, Z., Zhang, T., Duan, J., and Zhang, P.: Scanning vertical
distributions of typical aerosols along the Yangtze River using elastic lidar, Science of The Total Environment, 628, 631-
641, 2018.

Fleischmann, O. C., Hartmann, M., Burrows, J. P., and Orphal, J.: New ultraviolet absorption cross-sections of BrO at
atmospheric temperatures measured by time-windowing Fourier transform spectroscopy, Journal of Photochemistry and
Photobiology A: Chemistry, 168, 117-132, 2004.

Friedfeld, S., Fraser, M., Ensor, K., Tribble, S., Rehle, D., Leleux, D., and Tittel, F.: Statistical analysis of primary and
secondary atmospheric formaldehyde, Atmospheric Environment, 36, 4767-4775, doi:10.1016/s1352-2310(02)00558-7,
2002.

Garcia, A. R., Volkamer, R., Molina, L. T., Molina, M. J., Samuelson, J., Mellqvist, J., Galle, B., Herndon, S. C., and Kolb,
C. E.: Separation of emitted and photochemical formaldehyde in Mexico City using a statistical analysis and a new pair of
gas-phase tracers, Atmospheric Chemistry And Physics, 6, 4545-4557, 2006.

Goldan, P. D., Parrish, D. D., Kuster, W. C., Trainer, M., McKeen, S. A., Holloway, J., Jobson, B. T., Sueper, D. T., and
Fehsenfeld, F. C.: Airborne measurements of isoprene, CO, and anthropogenic hydrocarbons and their implications,
Journal Of Geophysical Research-Atmospheres, 105, 9091-9105, doi:10.1029/1999jd900429, 2000.

Hönninger, G., Friedeburg, C. v., and Platt, U.: Multi axis differential optical absorption spectroscopy (MAX-DOAS),
Atmospheric Chemistry and Physics, 4, 231-254, 2004.

Heckel, A., Richter, A., Tarsu, T., Wittrock, F., Hak, C., Pundt, I., Junkermann, W., and Burrows, J.: MAX-DOAS
measurements of formaldehyde in the Po-Valley, Atmospheric Chemistry and Physics, 5, 909-918, 2005.

Hendrick, F., Müller, J.-F., Clémer, K., Wang, P., Mazière, M. D., Fayt, C., Gielen, C., Hermans, C., Ma, J., and Pinardi, G.:
Four years of ground-based MAX-DOAS observations of HONO and NO_2 in the Beijing area, Atmospheric Chemistry

and Physics, 14, 765-781, 2014.

Huang, C., Chen, C., Li, L., Cheng, Z., Wang, H., Huang, H., Streets, D., Wang, Y., Zhang, G., and Chen, Y.: Emission inventory of anthropogenic air pollutants and VOC species in the Yangtze River Delta region, China, Atmospheric Chemistry and Physics, 11, 4105-4120, 2011.

Ibrahim, O., Shaiganfar, R., Sinreich, R., Stein, T., Platt, U., and Wagner, T.: Car MAX-DOAS measurements around entire cities: quantification of NO_x emissions from the cities of Mannheim and Ludwigshafen (Germany), Atmospheric Measurement Techniques, 3, 709-721, 2010.

Johansson, M., Rivera, C., Foy, B. d., Lei, W., Song, J., Zhang, Y., Galle, B., and Molina, L.: Mobile mini-DOAS measurement of the outflow of NO_2 and HCHO from Mexico City, Atmospheric Chemistry and Physics, 9, 5647-5653, 2009.

Krotkov, N. A., McLinden, C. A., Li, C., Lamsal, L. N., Celarier, E. A., Marchenko, S. V., Swartz, W. H., Bucsela, E. J., Joiner, J., Duncan, B. N., Boersma, K. F., Veefkind, J. P., Levelt, P. F., Fioletov, V. E., Dickerson, R. R., He, H., Lu, Z., and Streets, D. G.: Aura OMI observations of regional SO_2 and NO_2 pollution changes from 2005 to 2015, Atmospheric Chemistry And Physics, 16, 4605-4629, doi:10.5194/acp-16-4605-2016, 2016.

Krotkov, N. A., Lamsal, L. N., Celarier, E. A., Swartz, W. H., Marchenko, S. V., Bucsela, E. J., Chan, K. L., Wenig, M., and Zara, M.: The version 3 OMI NO_2 standard product, Atmos. Meas. Tech., 10, 3133-3149, doi:10.5194/amt-10-3133-2017, 2017.

Kuhlmann, G., Hartl, A., Cheung, H. M., Lam, Y. F., and Wenig, M. O.: A novel gridding algorithm to create regional trace gas maps from satellite observations, Atmos. Meas. Tech., 7, 451-467, doi:10.5194/amt-7-451-2014, 2014.

Lee, C., Richter, A., Lee, H., Kim, Y. J., Burrows, J. P., Lee, Y. G., and Choi, B. C.: Impact of transport of sulfur dioxide from the Asian continent on the air quality over Korea during May 2005, Atmospheric Environment, 42, 1461-1475, 2008.

Lee, D. S., Kohler, I., Grobler, E., Rohrer, F., Sausen, R., GallardoKlenner, L., Olivier, J. G. J., Dentener, F. J., and Bouwman, A. F.: Estimations of global NO_x emissions and their uncertainties, Atmospheric Environment, 31, 1735-1749, doi:10.1016/s1352-2310(96)00327-5, 1997.

Lei, W., Zavala, M., de Foy, B., Volkamer, R., Molina, M. J., and Molina, L. T.: Impact of primary formaldehyde on air pollution in the Mexico City Metropolitan Area, Atmospheric Chemistry And Physics, 9, 2607-2618, 2009.

Levelt, P. F., van den Oord, G. H., Dobber, M. R., Malkki, A., Visser, H., de Vries, J., Stammes, P., Lundell, J. O., and Saari, H.: The ozone monitoring instrument, IEEE Transactions on geoscience and remote sensing, 44, 1093-1101, 2006.

Li, A., Zhang, J., Xie, P., Hu, Z., Xu, J., Mou, F., Wu, F., Liu, J., and Liu, W.: Variation of temporal and spatial patterns of NO_2 in Beijing using OMI and mobile DOAS, Science China-Chemistry, 58, 1367-1376, doi:10.1007/s11426-015-5459-x, 2015.

Li, Y., Shao, M., Lu, S., Chang, C.-C., and Dasgupta, P. K.: Variations and sources of ambient formaldehyde for the 2008 Beijing Olympic games, Atmospheric Environment, 44, 2632-2639, 2010.

Ling, Z., Zhao, J., Fan, S., and Wang, X.: Sources of formaldehyde and their contributions to photochemical O_3 formation at

an urban site in the Pearl River Delta, southern China, Chemosphere, 168, 1293-1301, 2017.

Liu, H., Liu, C., Xie, Z., Li, Y., Huang, X., Wang, S., Xu, J., and Xie, P.: A paradox for air pollution controlling in China revealed by "APEC Blue" and "Parade Blue", Scientific Reports, 6, doi:10.1038/srep34408, 2016.

Ma, Y., Diao, Y., Zhang, B., Wang, W., Ren, X., Yang, D., Wang, M., Shi, X., and Zheng, J.: Detection of formaldehyde
620   emissions from an industrial zone in the Yangtze River Delta region of China using a proton transfer reaction ion-drift chemical ionization mass spectrometer, Atmospheric Measurement Techniques, 9, 6101-6116, doi:10.5194/amt-9-6101-2016, 2016.

Mallik, C., and Lal, S.: Seasonal characteristics of SO_2, NO_2, and CO emissions in and around the Indo-Gangetic Plain, Environmental Monitoring And Assessment, 186, 1295-1310, doi:10.1007/s10661-013-3458-y, 2014.

625   Mead, M., Popoola, O., Stewart, G., Landshoff, P., Calleja, M., Hayes, M., Baldovi, J., McLeod, M., Hodgson, T., and Dicks, J.: The use of electrochemical sensors for monitoring urban air quality in low-cost, high-density networks, Atmospheric Environment, 70, 186-203, 2013.

Meller, R., and Moortgat, G. K.: Temperature dependence of the absorption cross sections of formaldehyde between 223 and 323 K in the wavelength range 225-375 nm, Journal of Geophysical Research: Atmospheres, 105, 7089-7101, 2000.

630   Miller, S. M., Matross, D. M., Andrews, A. E., Millet, D. B., Longo, M., Gottlieb, E. W., Hirsch, A. I., Gerbig, C., Lin, J. C., Daube, B. C., Hudman, R. C., Dias, P. L. S., Chow, V. Y., and Wofsy, S. C.: Sources of carbon monoxide and formaldehyde in North America determined from high-resolution atmospheric data, Atmospheric Chemistry And Physics, 8, 7673-7696, 2008.

Parrish, D., Ryerson, T., Mellqvist, J., Johansson, J., Fried, A., Richter, D., Walega, J., Washenfelder, R. d., De Gouw, J.,
635   and Peischl, J.: Primary and secondary sources of formaldehyde in urban atmospheres: Houston Texas region, Atmospheric Chemistry and Physics, 12, 3273-3288, 2012.

Peters, E., Wittrock, F., Großmann, K., Frieß, U., Richter, A., and Burrows, J.: Formaldehyde and nitrogen dioxide over the remote western Pacific Ocean: SCIAMACHY and GOME-2 validation using ship-based MAX-DOAS observations, Atmospheric Chemistry and Physics, 12, 11179-11197, 2012.

640   Pinker, R., Frouin, R., and Li, Z.: A review of satellite methods to derive surface shortwave irradiance, Remote Sensing of Environment, 51, 108-124, 1995.

Platt, U., and Stutz, J.: Differential absorption spectroscopy: Principles and Applications, Springer, Berlin, 2008.

Possanzini, M., Di Palo, V., and Cecinato, A.: Sources and photodecomposition of formaldehyde and acetaldehyde in Rome ambient air, Atmospheric Environment, 36, 3195-3201, 2002.

645   Rozanov, A., Rozanov, V., Buchwitz, M., Kokhanovsky, A., and Burrows, J.: SCIATRAN 2.0-A new radiative transfer model for geophysical applications in the 175-2400nm spectral region, Advances in Space Research, 36, 1015-1019, 2005.

Schreier, S., Peters, E., Richter, A., Lampel, J., Wittrock, F., and Burrows, J.: Ship-based MAX-DOAS measurements of tropospheric NO_2 and SO_2 in the South China and Sulu Sea, Atmospheric Environment, 102, 331-343, 2015.

Serdyuchenko, A., Gorshelev, V., Weber, M., Chehade, W., and Burrows, J. P.: High spectral resolution ozone absorption

650   cross-sections - Part 2: Temperature dependence, Atmospheric Measurement Techniques, 7, 625-636, doi:10.5194/amt-7-625-2014, 2014.

Shaiganfar, R., Beirle, S., Sharma, M., Chauhan, A., Singh, R. P., and Wagner, T.: Estimation of NO_x emissions from Delhi using Car MAX-DOAS observations and comparison with OMI satellite data, Atmospheric Chemistry and Physics, 11, 10871-10887, 2011.

655   Shi, Y., Xia, Y.-f., Lu, B.-h., Liu, N., Zhang, L., Li, S.-j., and Li, W.: Emission inventory and trends of NO_x for China, 2000-2020, Journal of Zhejiang University Science A, 15, 454-464, 2014.

Sinreich, R., Coburn, S., Dix, B., and Volkamer, R.: Ship-based detection of glyoxal over the remote tropical Pacific Ocean, Atmospheric Chemistry and Physics, 10, 11359-11371, 2010.

Solomon, S., Schmeltekopf, A. L., and Sanders, R. W.: On the interpretation of zenith sky absorption measurements, Journal
660   of Geophysical Research, 92, 8311-8319, 1987.

Stein, A., Draxler, R. R., Rolph, G. D., Stunder, B. J., Cohen, M., and Ngan, F.: NOAA's HYSPLIT atmospheric transport and dispersion modeling system, Bulletin of the American Meteorological Society, 96, 2059-2077, 2015.

Su, W., Liu, C., Hu, Q., Fan, G., Xie, Z., Huang, X., Zhang, T., Chen, Z., Dong, Y., and Ji, X.: Characterization of ozone in the lower troposphere during the 2016 G20 conference in Hangzhou, Scientific reports, 7, 17368, 2017.

665   Takashima, H., Irie, H., Kanaya, Y., and Syamsudin, F.: NO_2 observations over the western Pacific and Indian Ocean by MAX-DOAS on Kaiyo, a Japanese research vessel, Atmospheric Measurement Techniques, 5, 2351-2360, 2012.

Thalman, R., and Volkamer, R.: Temperature dependent absorption cross-sections of O_2-O_2 collision pairs between 340 and 630 nm and at atmospherically relevant pressure, Physical Chemistry Chemical Physics, 15, 15371-15381, doi:10.1039/c3cp50968k, 2013.

670   Vandaele, A. C., Hermans, C., Simon, P. C., Carleer, M., Colin, R., Fally, S., Merienne, M.-F., Jenouvrier, A., and Coquart, B.: Measurements of the NO_2 absorption cross-section from 42000 cm^{-1} to 10000 cm^{-1} (238-1000 nm) at 220 K and 294 K, Journal of Quantitative Spectroscopy and Radiative Transfer, 59, 171-184, 1998.

Vandaele, A. C., Hermans, C., and Fally, S.: Fourier transform measurements of SO_2 absorption cross sections: II.: Temperature dependence in the 29000-44000 cm^{-1} (227-345 nm) region, Journal of Quantitative Spectroscopy and
675   Radiative Transfer, 110, 2115-2126, 2009.

Wagner, T., Burrows, J., Deutschmann, T., Dix, B., Friedeburg, C. v., Frieß, U., Hendrick, F., Heue, K.-P., Irie, H., and Iwabuchi, H.: Comparison of box-air-mass-factors and radiances for Multiple-Axis Differential Optical Absorption Spectroscopy (MAX-DOAS) geometries calculated from different UV/visible radiative transfer models, Atmospheric Chemistry and Physics, 7, 1809-1833, 2007.

680   Wagner, T., Ibrahim, O., Shaiganfar, R., and Platt, U.: Mobile MAX-DOAS observations of tropospheric trace gases, Atmospheric Measurement Techniques, 3, 129-140, 2010.

Wang, M., Chen, W., Shao, M., Lu, S., Zeng, L., and Hu, M.: Investigation of carbonyl compound sources at a rural site in the Yangtze River Delta region of China, Journal Of Environmental Sciences, 28, 128-136, doi:10.1016/j.jes.2014.12.001,

2015.

685 Wang, S., Zhang, Q., Streets, D., He, K., Martin, R., Lamsal, L., Chen, D., Lei, Y., and Lu, Z.: Growth in NO_x emissions from power plants in China: bottom-up estimates and satellite observations, Atmospheric Chemistry and Physics, 12, 4429-4447, 2012a.

Wang, S., Zhou, B., Wang, Z., Yang, S., Hao, N., Valks, P., Trautmann, T., and Chen, L.: Remote sensing of NO_2 emission from the central urban area of Shanghai (China) using the mobile DOAS technique, Journal Of Geophysical Research-

690 Atmospheres, 117, doi:10.1029/2011jd016983, 2012b.

Wang, T., Hendrick, F., Wang, P., Tang, G., Clémer, K., Yu, H., Fayt, C., Hermans, C., Gielen, C., and Müller, J.-F.: Evaluation of tropospheric SO_2 retrieved from MAX-DOAS measurements in Xianghe, China, Atmospheric Chemistry and Physics, 14, 11149-11164, 2014.

Wang, Y., Lampel, J., Xie, P., Beirle, S., Li, A., Wu, D., and Wagner, T.: Ground-based MAX-DOAS observations of

695 tropospheric aerosols, NO_2, SO_2 and HCHO in Wuxi, China, from 2011 to 2014, Atmospheric Chemistry And Physics, 17, 2189-2215, doi:10.5194/acp-17-2189-2017, 2017.

Wood, E. C., Canagaratna, M. R., Herndon, S. C., Onasch, T. B., Kolb, C. E., Worsnop, D. R., Kroll, J. H., Knighton, W. B., Seila, R., Zavala, M., Molina, L. T., DeCarlo, P. F., Jimenez, J. L., Weinheimer, A. J., Knapp, D. J., Jobson, B. T., Stutz, J., Kuster, W. C., and Williams, E. J.: Investigation of the correlation between odd oxygen and secondary organic aerosol

700 in Mexico City and Houston, Atmospheric Chemistry And Physics, 10, 8947-8968, doi:10.5194/acp-10-8947-2010, 2010.

Wu, F.-C., Li, A., Xie, P.-H., Chen, H., Ling, L.-Y., Xu, J., Mou, F.-S., Zhang, J., Shen, J.-C., Liu, J.-G., and Liu, W.-Q.: Dectection and distribution of tropospheric NO_2 vertical column density based on mobile multi-axis differential optical absorption spectroscopy, Acta Physica Sinica, 64, doi:10.7498/aps.64.114211, 2015.

Wu, F., Xie, P., Li, A., Chan, K., Hartl, A., Wang, Y., Si, F., Zeng, Y., Qin, M., and Xu, J.: Observations of SO_2 and NO_2 by

705 mobile DOAS in the Guangzhou eastern area during the Asian Games 2010, Atmospheric Measurement Techniques, 6, 2277-2292, doi:10.5194/amt-6-2277-2013, 2013.

Xia, Y., Zhao, Y., and Nielsen, C. P.: Benefits of China's efforts in gaseous pollutant control indicated by the bottom-up emissions and satellite observations 2000–2014, Atmospheric Environment, 136, 43-53, 2016.

Xing, C., Liu, C., Wang, S., Chan, K. L., Gao, Y., Huang, X., Su, W., Zhang, C., Dong, Y., and Fan, G.: Observations of the

710 vertical distributions of summertime atmospheric pollutants and the corresponding ozone production in Shanghai, China, Atmospheric Chemistry and Physics, 17, 14275-14289, 2017.

Zhang, L., Lee, C. S., Zhang, R., and Chen, L.: Spatial and temporal evaluation of long term trend (2005-2014) of OMI retrieved NO_2 and SO_2 concentrations in Henan Province, China, Atmospheric Environment, 154, 151-166, doi:10.1016/j.atmosenv.2016.11.067, 2017.

715 Zhao, Y., Wang, S., Duan, L., Lei, Y., Cao, P., and Hao, J.: Primary air pollutant emissions of coal-fired power plants in China: Current status and future prediction, Atmospheric Environment, 42, 8442-8452, 2008.

Table 1. Weather and viewing conditions during Yangtze River campaign from 22 November to 4 December, 2015. Interruption of the ship based MAX-DOAS is also listed.

Period	Conditions		
22-25 November	Rain and occasional fog occurred in the morning and night		
26-27 November	Improving weather and viewing conditions, sunny		
28 November	Occasional light rain and partly cloudy around noon		
29 November	Haze		
30 November	Partly cloudy		
1-2 December	Haze		
3-4 December	Good viewing conditions, almost clear sky		
Interruption event	Start time (yyyy/mm/dd, UTC + 8 h)	End time (yyyy/mm/dd, UTC + 8 h)	Reason for interruption
1	2015/11/22 11:00	2015/11/22 14:25	power outages
2	2015/11/25 7:00	2015/11/25 18:00	frequent power outages all day long
3	2015/11/26 11:40	2015/11/26 15:00	instrumental problems

720

Table 2. Summary of the DOAS retrieval settings used for the NO_2, SO_2, and HCHO slant column densities retrieval.

Parameter	Data source	Fitting internal (nm)		
		NO_2	SO_2	HCHO
Wavelength range		338-368 nm	308-314 nm	336.5-359 nm
NO_2	Vandaele et al. (1998), 220K, 294K, I_0-correction* (SCD of 10^{17} molecules/cm^2)	√	√ (only 294K)	√ (only 294K)
SO_2	Vandaele et al. (2009), 298K	×	√	×
HCHO	Meller and Moortgat (2000), 297K	√	×	√
O_3	Serdyuchenko et al. (2014), 223K, 243K, I_0-correction* (SCD of 10^{20} molecules/cm^2)	√	√	√
O_4	Thalman and Volkamer (2013), 293K	√	×	√
BrO	Fleischmann et al. (2004), 223K	√	×	√
Ring	Ring spectra calculated with QDOAS according to Chance and Spurr (1997)	√	√	√
Polynomial degree		Order 5	Order 5	Order 5
Intensity offset		Constant	Order 1	Order 1
Wavelength calibration	Based on a high resolution solar reference spectrum (SAO2010 solar spectra) (Chance and Kurucz, 2010)			

*Solar I_0-correction (Aliwell et al., 2002)

725 **Table 3.** Coefficients of the multiple linear regression and the correlation coefficient (R) for the measured and modeled HCHO in Eq. (15). β_1 represents the emission ratio of HCHO with respect to CO. β_2 denotes the portion of HCHO from photochemical production, while β_0 represents HCHO background concentration which is fixed to 1 ppbv.

Date (yyyy/mm/dd)	β_1	β_2	β_0	R	N.Obs
2015/11/26	0.0165±0.0083	0.0765±0.0323	1.0	0.7937	80
2015/12/03	0.0312±0.0097	0.1149±0.0514	1.0	0.7746	139

730
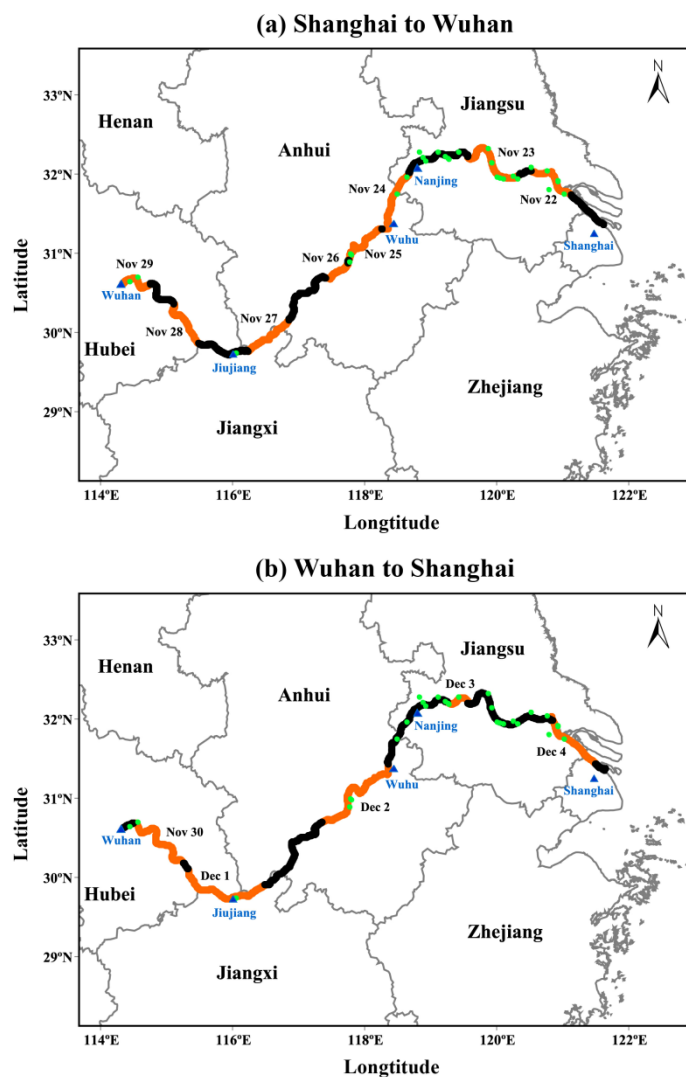
Figure 1. The ship tracks of (a) the departing journey (from Shanghai to Wuhan) and (b) the returning journey (from Wuhan to Shanghai). The sections of the cruise track highlighted in orange indicate the period of MAX-DOAS observations. The green dots represent the major power plants along the Yangtze River.

735
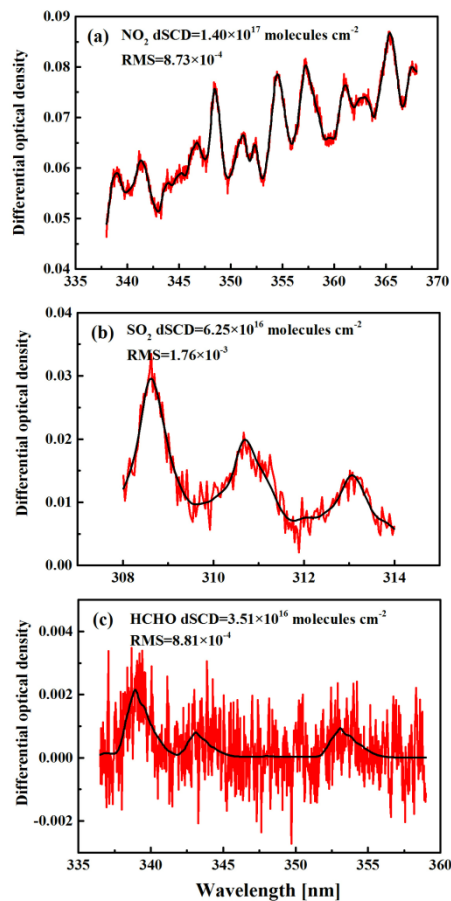
Figure 2. An example of DOAS fit for (a) NO₂, (b) SO₂, and (c) HCHO. The spectrum was taken on 1 December 2015 at 14:02 LT with elevation angle of 30°. Red lines show the measured atmospheric spectrum after all other absorbers have been subtracted, and the black line shows the scaled reference absorption cross section.

740
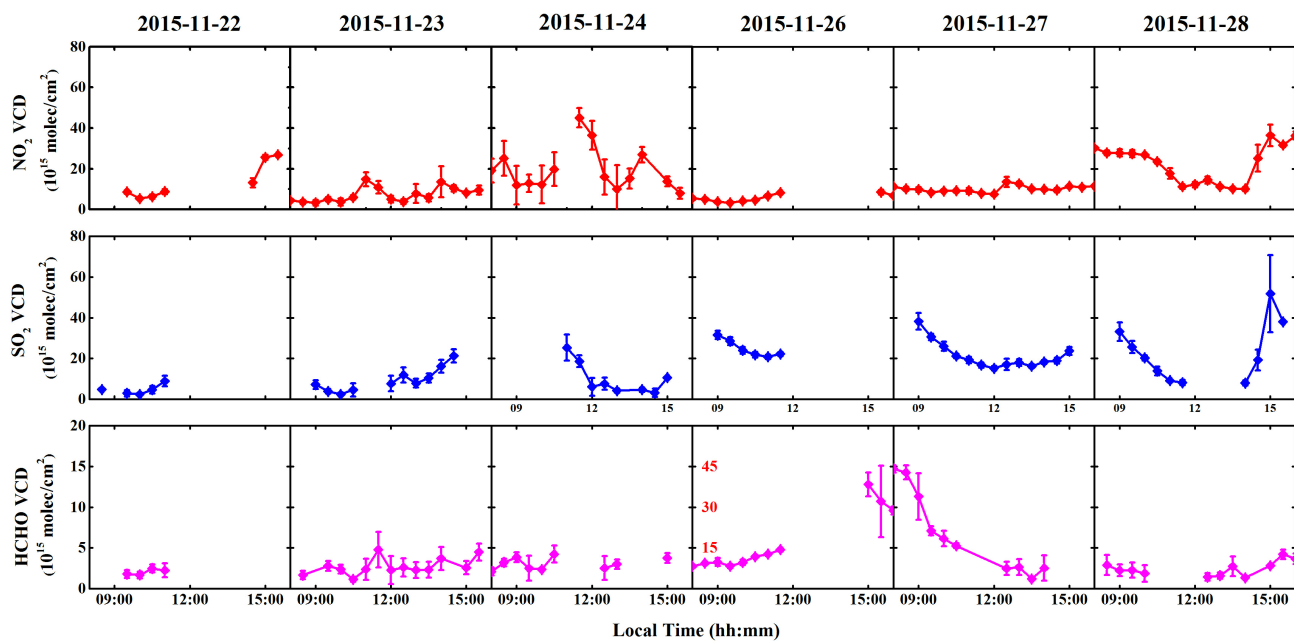
Figure 3. Time series of tropospheric NO$_2$ (upper panels), SO$_2$ (middle panels), and HCHO (lower panels) vertical column densities (VCDs) from 22 November to 28 November. The error bars refer to the 1σ variation of the measurement.

Notes: The data were half-hour averages and individual measurements taken under unfavorable wind directions have been filtered before averaging. No data presented on 25 November due to frequent power outages. The y-axis scale of HCHO on 26 November is different (y-axis scale in red).
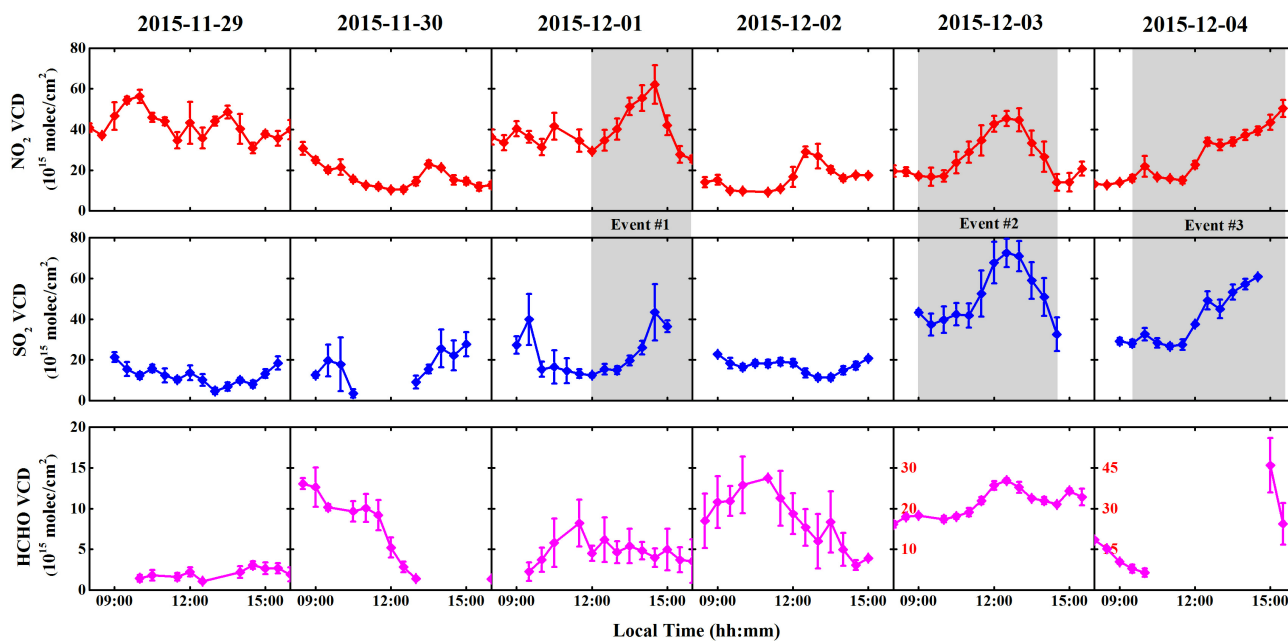
Figure 4. Continue of Fig. 3, but for the time series of tropospheric NO$_2$ (upper panels), SO$_2$ (middle panels), and HCHO (lower panels) vertical column densities (VCDs) from 22 November to 28 November. The gray area highlighted the episode periods which NO$_2$ and SO$_2$ showed synchronous growth.

Notes: The y-axis scale of HCHO on 3-4 December is different (y-axis scale in red).
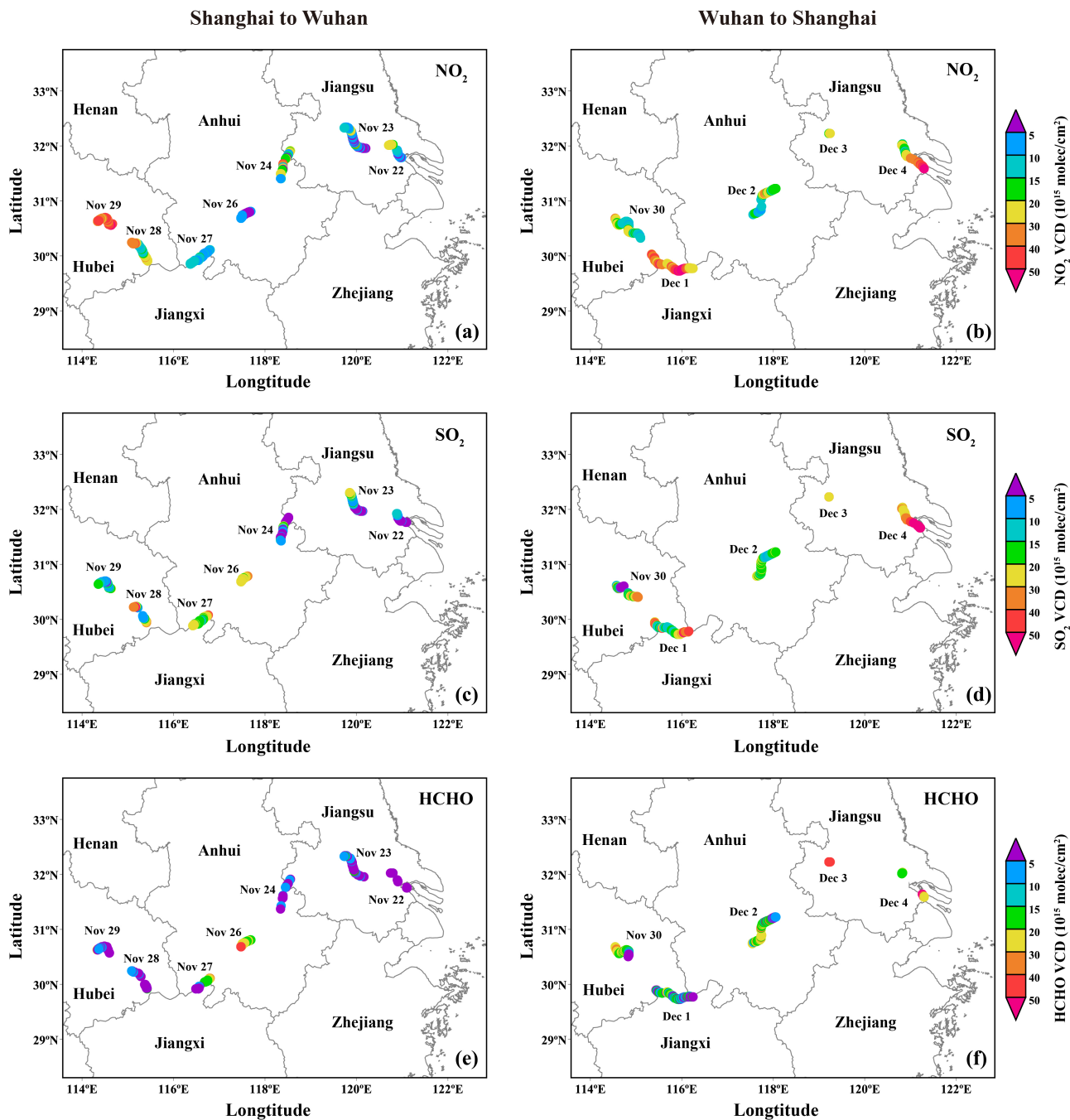
Figure 5. Spatial distribution of tropospheric NO₂ (upper panels), SO₂ (middle panels), and HCHO (lower panels) VCDs along the departing route (left panels, from Shanghai to Wuhan) and returning route (right panels, from Wuhan to Shanghai). Notes: The ship was anchored at Yizheng Marine department on 3 December 2015.
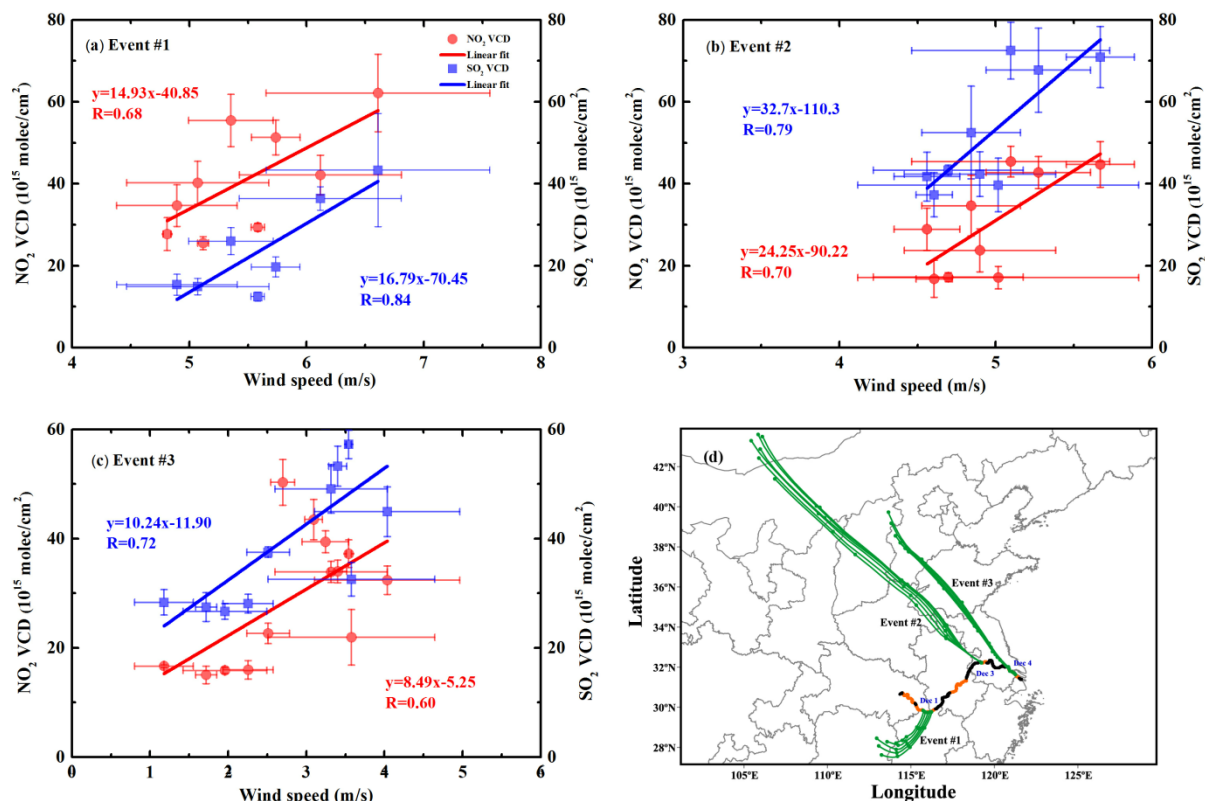
Figure 6. (a-c) Correlation analysis of ship-based MAX-DOAS VCDs (red circle shows the NO_2 VCDs and blue square shows the SO_2 VCDs) and wind speed for three high VCDs events. (d) Yangtze River Cruise Track and 24 h backward trajectories calculated by the NOAA HYSPLIT model for three events (green marks indicate starting point, −6, −12, −18 and −24 h, respectively). The data were half-hour averages. The error bars show the 1σ standard deviations of mobile DOAS VCDs and wind speed.
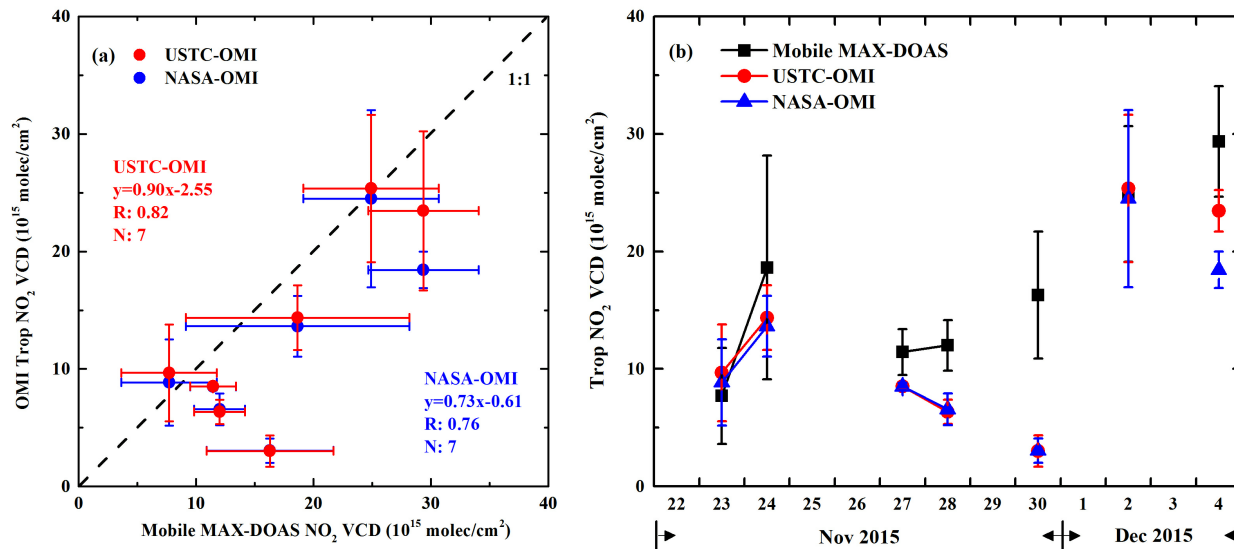
Figure 7. (a) Correlation analysis and (b) time series of tropospheric NO_2 VCDs measured by ship-based MAX-DOAS and OMI during Yangtze River campaign. MAX-DOAS data (black markers) are temporally averaged around the USTC OMI and NASA OMI overpass time (red and blue markers, respectively), while the OMI data are spatially averaged within 20 km radius around the ship's averaged position. The error bars show the 1σ standard deviations of ship-based MAX-DOAS and OMI data.
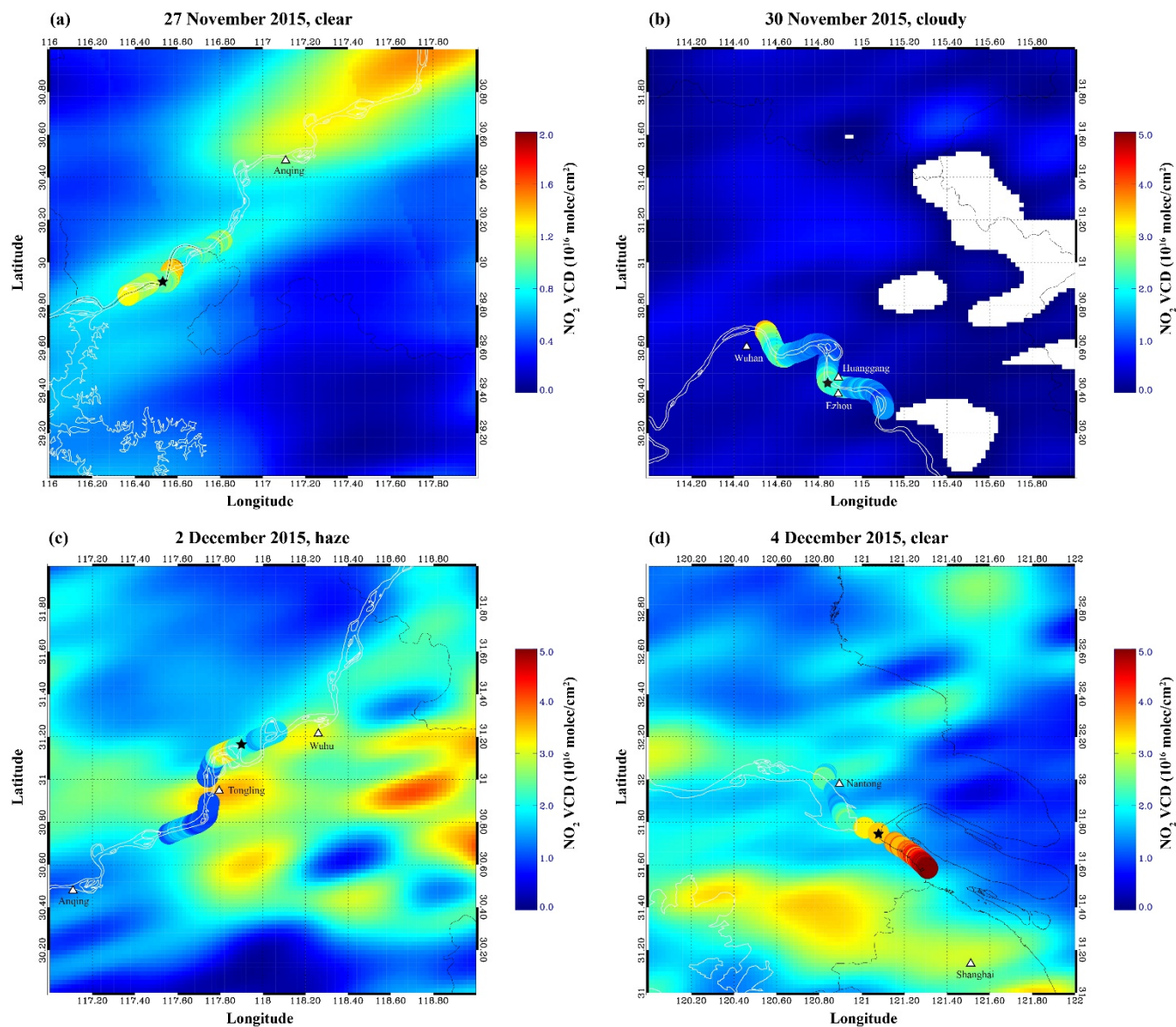
Figure 8. Spatial pattern of tropospheric NO₂ VCD measured by ship-based MAX-DOAS and OMI during four typical days
775 within the Yangtze River campaign. The color-coded circle indicates the ship-based MAX-DOAS observations. Each plot
show example for relatively clear (a and d), cloudy (b), and haze (c) metrological conditions along Yangtze River. The star
symbols indicate the ship position during the OMI overpass time (~13:45 LT). The colorbar scale of each panel is different.
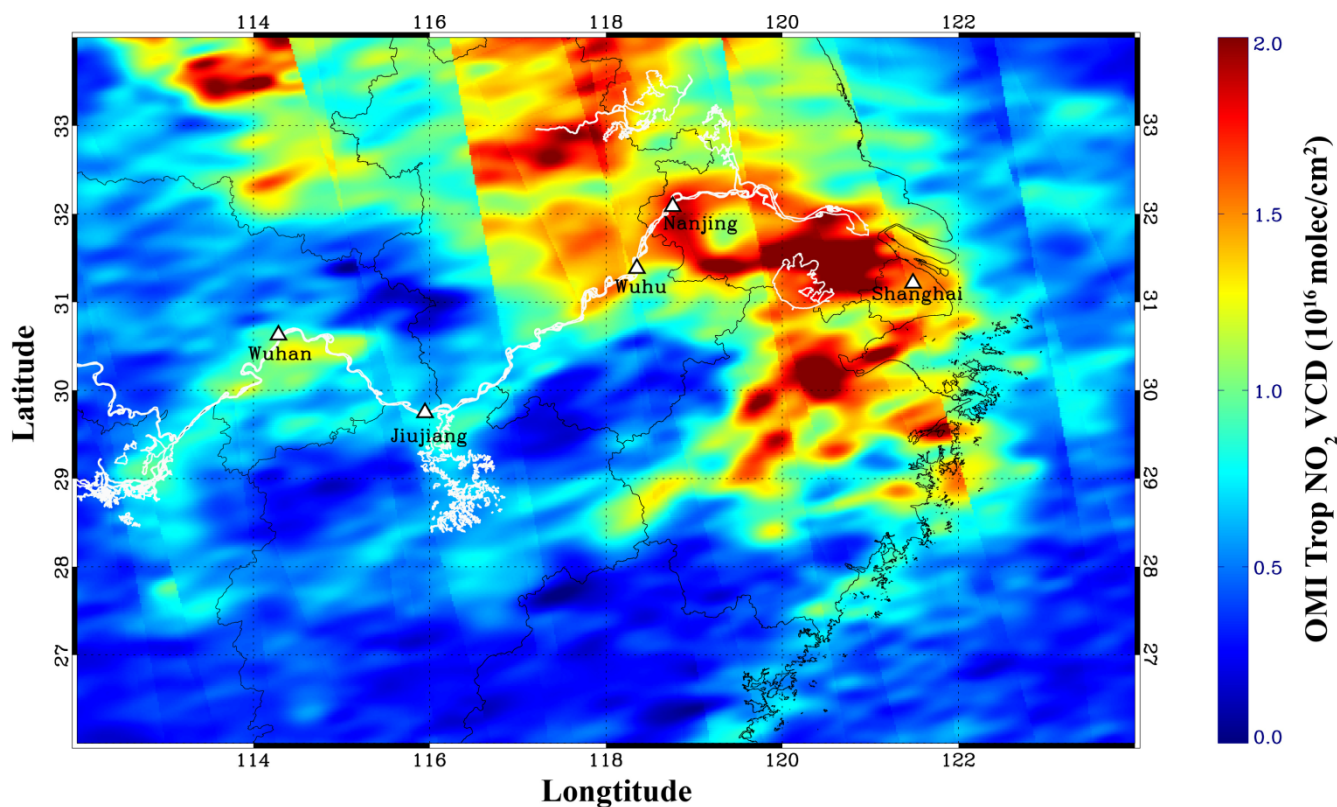
780 **Figure 9.** The spatial distribution of averaged tropospheric NO$_2$ VCDs measured by OMI during Yangtze River campaign (22 November to 4 December, 2015).
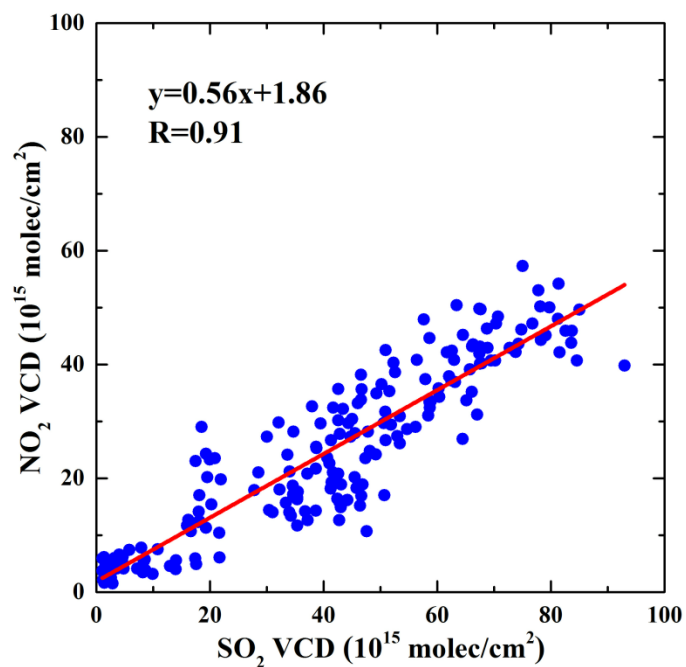
Figure 10. Scatter plot of NO₂ and SO₂ VCDs data around power plants along the Yangtze River. NO₂ and SO₂ VCDs measured within 2 km of the power plants are used for the analysis.
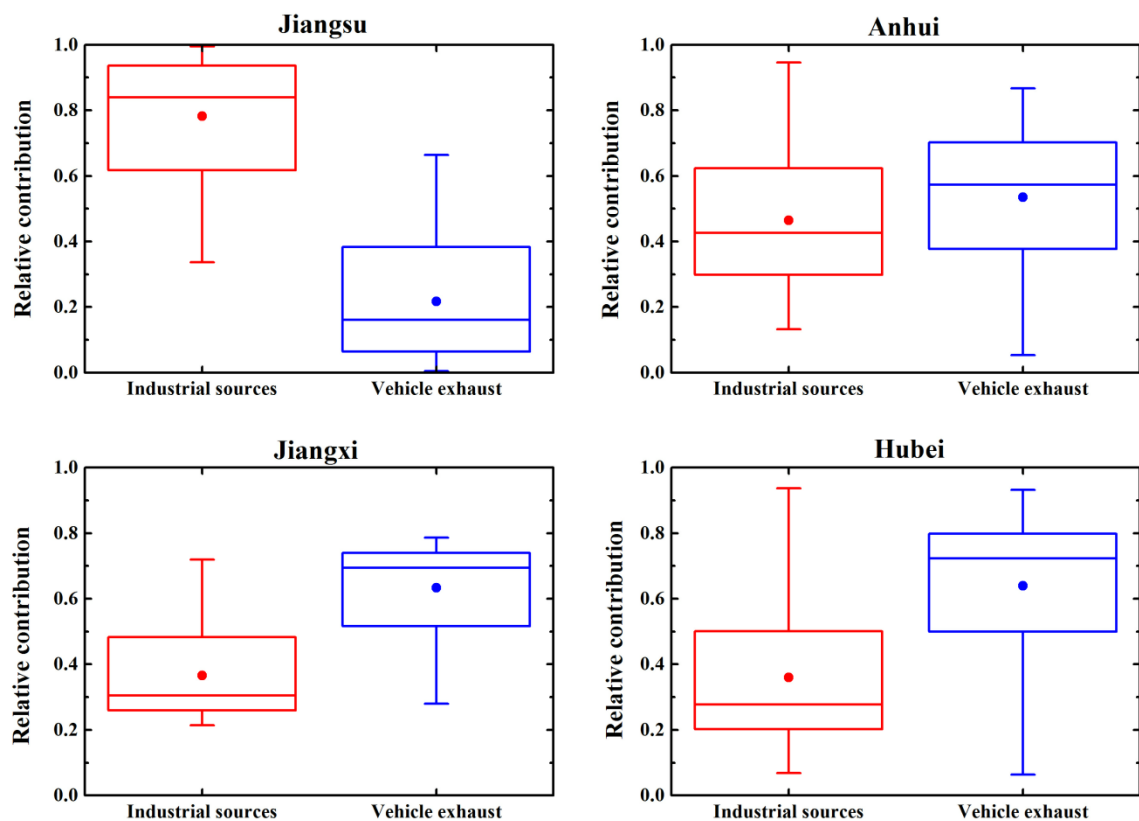
Figure 11. Relative contributions of industrial sources and vehicle exhaust to the ambient NO$_2$ levels over the four provinces.

Notes: the bottom and top of the box represent the 25th and 75th percentiles, respectively; the line within the box represent

790   the median; the dot represents the mean; the whiskers below and above the box stands for the 10th and 90th percentiles.
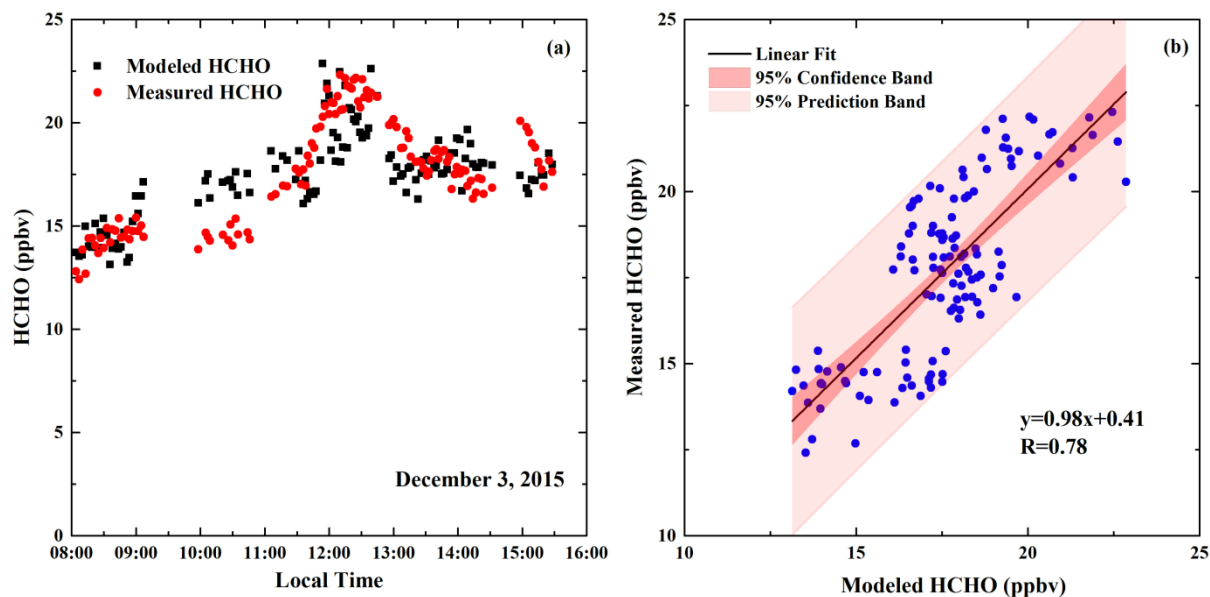
Figure 12. Comparison of the measured and modeled HCHO values from multiple linear regression on 3 December 2015. The left panel shows the modeled and measured HCHO time series. The right panel shows the linear correlation between the modeled and measured HCHO concentrations. The black solid line indicates the linear regression. The red and pink areas denote the 95% confidence interval and the 95% prediction, respectively.
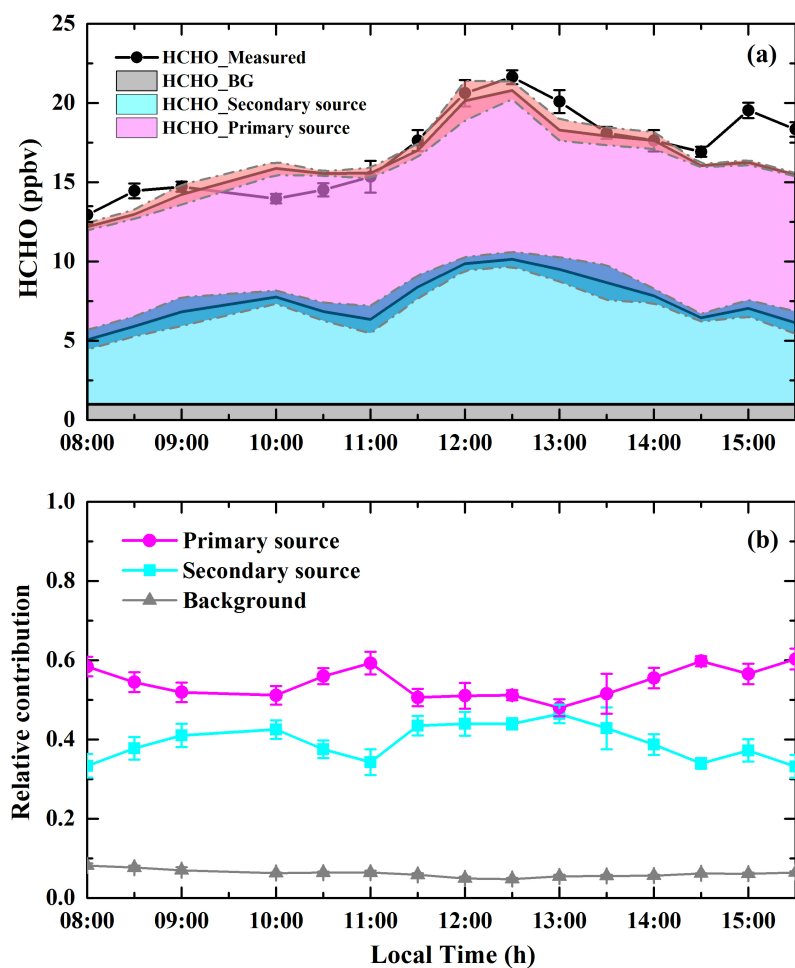
Figure 13. Time series of absolute (upper) and relative (lower) contribution of primary source, secondary source, and atmospheric background to ambient HCHO level on 3 December 2015. The error bars refer to the 1σstandard variations of the absolute (upper, error bars with fill area) and relative (lower) contribution of primary source, secondary source, and atmospheric background to ambient HCHO.